Non-Hermitian Phenomena
in the Trimer Su-Schrieffer-Heeger Model

Division of Solid State Physics
Duration: 2 months
June, 2024

LUND
UNIVERSITY

Bachelor Thesis
Authored by Elton Giacomelli Nilsson
Supervised by Dr. Flore Kunst and Prof. Martin Leijnse

Abstract

The trimer Su-Schrieffer-Heeger (SSH3) model extends the traditional Su-Schrieffer-Heeger model by incorporating an additional lattice site per unit cell. Although it lacks chiral symmetry, the SSH3 model exhibits bulk-boundary correspondence (BBC) with topologically protected, localized edge states under open boundary conditions. This thesis investigates non-Hermitian phenomena in the anisotropic SSH3 model. Introducing anisotropy in the hopping amplitudes breaks the BBC, leading to the emergence of the non-Hermitian skin effect and exceptional points. Through a unitary transformation, the SSH3 model is mapped to a model with reciprocal hopping amplitudes and on-site dissipation, where the non-Hermitian skin effect nevertheless remains. An extensive analysis of exceptional points of order n (EPns) in the SSH3 model uncovers the existence of EP2s and EP3s, with EP2 lines connecting EP3s under chiral and particle-hole symmetry. EP3s are shown to occur only in the presence of chiral or sublattice symmetry. Additionally, analytical solutions for the boundary states are derived, and the biorthogonal framework is employed to examine the model's topological properties. The biorthogonal polarization is identified as a topological invariant that accurately predicts the localization of boundary states.

Acknowledgements

This thesis concludes my Bachelor's level research period at Lund University, distilling it into words and figures, yet unable to fully capture the formative conversations and experiences that shaped it. Partly out of nostalgia, with the knowledge that challenges often mellow into fond memories, I will attempt to preserve in ink the contributions of those who made the journey possible.

To settle my debts of gratitude, I must first thank my supervisor, Dr. Flore Kunst; it takes a remarkable person to invest time in student engagement while simultaneously leading an entire field of research. Working with someone so pedagogical, patient, and prolific has been an invaluable honor.

My gratitude extends to Prof. Martin Leijnse, who generously adopted the role of co-supervisor and never doubted my ability to deliver. I am also thankful to my examiner, Prof. Edouard Berrocal, whose compassion and understanding enabled me to complete this thesis.

To my parents, who have always been my most ardent supporters, I owe debts that can never be repaid. You stand at the root of all my achievements, and I hope to make you proud. In the same vein of support, my friends and colleagues deserve notice - for listening, sharing their knowledge, and providing distraction when needed.

In closing, I must acknowledge Mia, whose passion for topology inspired me down this path. After patiently entertaining my endless musings on Bloch Hamiltonians and exceptional points, the only honor I can impart is to dedicate this thesis to her.

Abbreviations

BBC - Bulk-boundary correspondence

BQM - Biorthogonal quantum mechanics

DOF - Degree of freedom

EP - Exceptional point

LP - Localization parameter

NH - Non-Hermitian

OBC - Open boundary conditions

PBC - Periodic boundary conditions

SSH - Su-Schrieffer-Heeger

TI - Topological insulator

Contents

1 Introduction

The earliest discovery of topological matter was the integer quantum Hall effect in 1980 [1]. In this later Nobel prize-awarded experiment, von Klitzing showed that the conductance of a two-dimensional electron system is quantized in units of e^2/h [2]. The integer factor was later understood to be the Chern number, a topological invariant related to the complex phase around loops in Hilbert space [3]. Following this initial discovery, the same features were generalized to realistic models without magnetic fields and in higher dimensions [4]. Models of topological insulators (TIs), a type of matter with an insulating bulk and topologically protected boundary states, were constructed and soon experimentally realized [5]. Far from being a mere theoretical exercise, topological insulators have already found applications in thermoelectrics [6] and lasing [7]. Moreover, Majorana fermions - emergent particles that are their own antiparticles - have been predicted [5] for TIs interacting with superconductors. The Majorana fermions, if experimentally realized, could lead to topological quantum computers that are protected from noise [4].

Theoretical work on non-Hermitian (NH) topological phenomena arose due to anomalous behavior in experiments with energy dissipation [8]. Unlike Hermitian operators, which are equal to their adjoint ($H = H^\dagger$), NH operators do not generally have real eigenvalues or conserved probabilities. Instead, NH operators often describe open systems with energy dissipation or influx [9]; their eigenvalues can be complex, and their eigenvectors are not generally orthogonal. The abundance of open systems therefore provides a strong incentive to study NH systems. Another reason is the novel phenomena that arise when Hermiticity is not enforced. Among the new features, the emergence of exceptional points (EPs), the proliferation of symmetries, and the generalization of orthogonality to biorthogonality are of particular interest to this thesis. EPs occur when eigenvalues and eigenvectors coalesce. In this thesis, a classification of EPs is adopted where orders are defined by the number of eigenvectors with a shared eigenvalue coalescing onto a single eigenvector. The notation employed for an EP of order n is EPn, such that an EP2 is a second-order exceptional point. For TIs, non-Hermiticity may cause a breakdown of the bulk-boundary correspondence, the feature of Hermitian TIs that connects the boundary states to a bulk invariant. Further, certain systems exhibit the NH skin effect, where many bulk eigenstates accumulate at the boundary. An improved understanding of these phenomena is leading to applications such as light funneling [10] and unidirectional lasing [11]. Unlike Hermitian systems, for which the dispersion around an eigenvalue degeneracy (also called a diabolical point) is linear, the dispersion around an EP behaves as some nth root. By tuning the system parameters to operate at an EP, the sensitivity of sensors can be enhanced, as has been experimentally validated [12], [13]. This enhancement is exemplified in Figure 1.1.

The quintessential example of a TI, both in the Hermitian and non-Hermitian context, is the one-dimensional Su-Schrieffer-Heeger model. The lattice consists of two sites per unit cell, with distinct amplitudes for intra- and inter-cell hopping. Despite its simplicity, the model exhibits the essential features of TIs and has seen experimental realization in optical and mechanical systems [14], [15]. While many modifications can be introduced to make the SSH chain non-Hermitian, this thesis will focus on the anisotropic model. In chapter 2, an introduction to the SSH model is provided along with the necessary background on symmetries, boundary states, and biorthogonal quantum mechanics. Chapter 3 then presents the anisotropic trimer SSH model (SSH3), the main focus of this thesis. The model extends the SSH model by introducing an extra lattice site to each unit cell. Current literature on the anisotropic SSH3 model has explored the symmetries of its Bloch Hamiltonian, examined the profiles of the boundary states, and attempted to introduce a topological invariant through Zak's phase [16]. This thesis elaborates on these studies with an original investigation through the biorthogonal framework. In section 3.4, exact boundary solutions are explicitly derived, extending on the presently available parameterized forms, and the biorthogonal polarization is for the first time evaluated

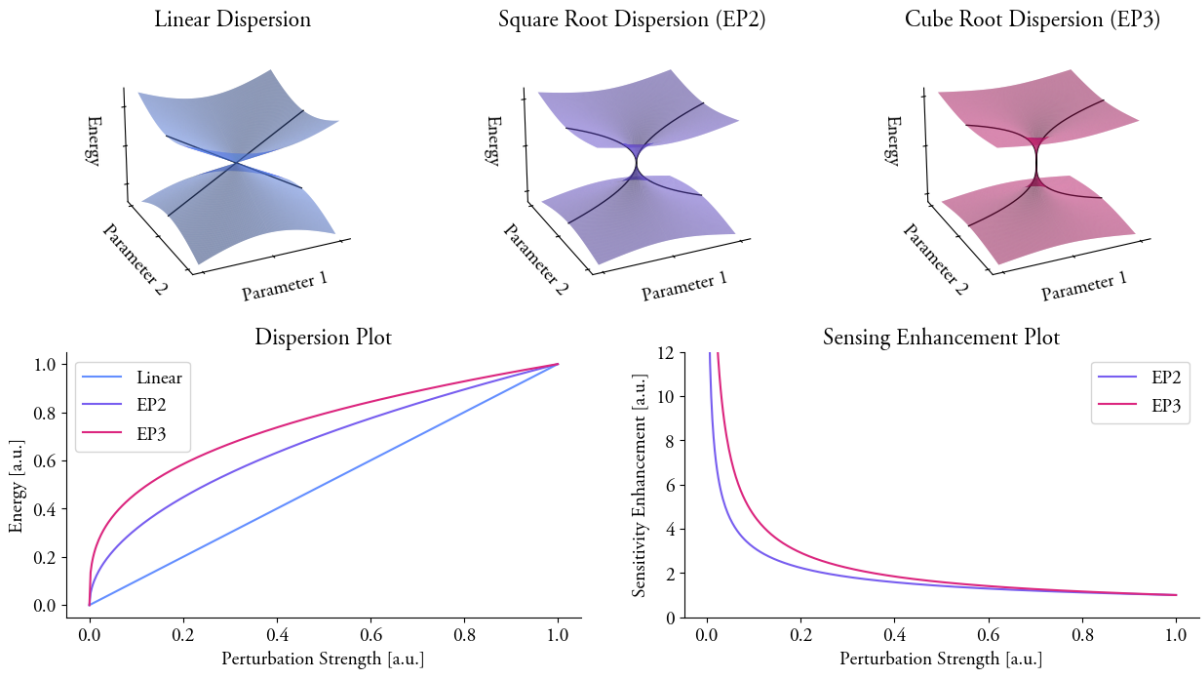

Figure 1.1: Qualitative illustration of how exceptional points can improve metrology. The upper panel shows the dispersion relation around a diabolical point, an EP2, and an EP3. The EP2 is depicted with a square root dispersion, while the EP3 has a cubic dispersion, although this is not a general rule. The figure is adapted and abstracted from experimental results in [12], [13]. The two bottom plots show the dispersion and sensing enhancement for a system operating at an EP. The perturbation strength captures the distance from the EP in the parameter space. Sensing enhancement is calculated relative to the linear dispersion.

as a topological invariant of the SSH3. The thesis also provides the first investigation into the occurrence of exceptional points in the SSH3 model. In section 3.6, a unitary transformation into a distinct model with on-site gain and dissipation is presented, where the NH skin effect is present despite reciprocal hopping amplitudes; this introduces further possibilities for experimental realization of the results. Finally, a discussion and outlook are provided in chapter 4.

2 Background

2.1 Symmetries

Following the work of Altand and Zirnbauer, Hermitian topological insulators are characterized by their symmetry constraints [17]. In particular, ten symmetry classes arise from the unique combinations of chiral symmetry (CS), time-reversal symmetry (TRS), and particle-hole symmetry (PHS). The presence of a symmetry depends on whether an operator exists that satisfies the relevant symmetry constraint. Chiral symmetry involves a unitary operator S satisfying the symmetry constraint

$$SH(\boldsymbol{k})S^{-1} = -H(\boldsymbol{k}).$$

Time-reversal symmetry is defined by

$$T_{\pm}H^{*}(-\boldsymbol{k})T_{\pm}^{-1} = H(\boldsymbol{k}).$$

The subscript on the operator T denotes the sign of their square, $T_{\pm}T_{\pm}^{*} = \pm 1$. The negative sign for $\mathcal{T}_{-}$ requires particles of half-integer spin [18]; since this thesis concerns itself with spinless particles, the subscript will be dropped, understanding that T squares to 1. It can be shown from its effect on the Schrödinger equation that T has to be anti-unitary [19]. The anti-unitary property is defined by how the operator conjugates an inner product [20],

$$\langle A\phi|A\psi\rangle = \langle\phi|\psi\rangle^{*} = \langle\psi|\phi\rangle.$$

Any anti-unitary operator can be decomposed into a conjugation operator K and a unitary operator U so that $A = UK$. Scalars operated on are therefore transformed by complex conjugation. For time reversal with spinless particles, the unitary transformation is simply the identity.

Finally, the particle-hole symmetry constraint is

$$CH^{*}(-\boldsymbol{k})C^{-1} = -H(\boldsymbol{k}).$$

When extending our studies to non-Hermitian systems, new symmetries are introduced. As a consequence, the number of symmetry classes is increased to 38 [21]. The reason for this accumulated richness is partly the plurality of generalizations of Hermitian symmetries. Chiral symmetry, for example, has the alternative definition

$$SH^{\dagger}(\boldsymbol{k})S^{-1} = -H(\boldsymbol{k}).$$

For a Hermitian Hamiltonian, these definitions are equivalent. In the non-Hermitian framework, the latter equation is termed chiral symmetry and the earlier definition is renamed sublattice symmetry (SLS). TRS and PHS also bifurcate into one symmetry that maintains the complex conjugation, and one that substitutes it with transposition [8].

The other reason for a richer symmetry landscape is the introduction of pseudo-Hermiticity, a matrix similarity that ensures the eigenvalues are either real or constitute complex conjugate pairs. A related symmetry is parity-time (PT) symmetry, defined by the consecutive operations of time- and parity-reversal. PT symmetry implies pseudo-Hermiticity for finite systems [22]. The spectral properties of PT-symmetric operators have gained much traction since their introduction by Bender and Boettcher [23]. This is mainly due to how an entirely real spectrum can be obtained without satisfying the traditional axiom of Hermiticity. The symmetry is also

finding applications in optics, where it has been shown to enable unidirectional lasing and media invisibility [11], [24]. The symmetry constraint is

$$AH^*(\boldsymbol{k})A^{-1} = H(\boldsymbol{k}).$$

For each symmetry constraint, there exists a corresponding energy constraint. Taking SLS as an example, the set of energies $\{\varepsilon(k)\}$ must be the same set as $\{-\varepsilon(k)\}$. To demonstrate this, consider an eigenstate $|\phi_i\rangle$ of $H(k)$ with eigenvalue E_i. SLS implies that $S|\phi_i\rangle$ is an eigenstate of $H(k)$ with eigenvalue $-E_i$. This result is obtained by the following chains of equivalences:

$$\begin{aligned} & SH(k)S^{-1}S|\phi_i\rangle = SE_i|\phi_i\rangle \\ \iff & -H(k)S|\phi_i\rangle = E_iS|\phi_i\rangle \\ \iff & H(k)S|\phi_i\rangle = -E_iS|\phi_i\rangle\,. \end{aligned}$$

Similar derivations can be made for the other symmetries. All relevant symmetries and their corresponding symmetry- and energy-constraints are summarized in Table 2.1.

Table 2.1: Symmetries and their corresponding symmetry- and energy-constraints, adapted from [25].

Symmetry	Symmetry Constraint	Energy Constraint
Chiral (CS)	$SH^\dagger(\boldsymbol{k})S^{-1} = -H(\boldsymbol{k})$	$\{\varepsilon(k)\} = \{-\varepsilon^*(k)\}$
Sublattice (SLS)	$SH(\boldsymbol{k})S^{-1} = -H(\boldsymbol{k})$	$\{\varepsilon(k)\} = \{-\varepsilon(k)\}$
Time-reversal (TRS)	$TH^*(-\boldsymbol{k})T^{-1} = H(\boldsymbol{k})$	$\{\varepsilon(k)\} = \{\varepsilon^*(-k)\}$
Particle-hole (PHS)	$CH^*(-\boldsymbol{k})C^{-1} = -H(\boldsymbol{k})$	$\{\varepsilon(k)\} = \{-\varepsilon^*(-k)\}$
Parity-time (PT)	$AH^*(\boldsymbol{k})A^{-1} = H(\boldsymbol{k})$	$\{\varepsilon(k)\} = \{\varepsilon^*(k)\}$

2.2 Boundary states

The central feature of topological insulators is the topologically protected boundary states. For this reason, it will be useful to introduce a general lattice model with exact boundary state solutions. The model presented by Kunst et al. [26], [27], which also covers higher-dimensional structures, serves as the basis for the following section.

We consider a one-dimensional lattice as presented in Figure 2.1, with alternating sites X and Y, and only nearest-neighbor hopping. For the greatest generalizability, the original model is extended to allow for staggered hopping amplitudes $h^\dagger_{O;+} \neq h^\dagger_{U;+}$. The lattice is restricted to both start and end with an X-site. The X-sites have n internal degrees of freedom (DOF) while Y-sites only have one. Later on, the internal DOFs will be conceived of as lattice sites. The Hamiltonian can be written as

$$\mathcal{H}_M = \begin{pmatrix} h_X & h_{O;+} & 0 & 0 & 0 \\ h^\dagger_{U;+} & h_Y & h^\dagger_{O;-} & 0 & 0 \\ 0 & h_{U;-} & h_X & \dots & 0 \\ 0 & 0 & \vdots & \ddots & h^\dagger_{O;-} \\ 0 & 0 & 0 & h_{U;-} & h_X \end{pmatrix}, \tag{2.1}$$

where h_X and h_Y represent the Hamiltonians of the respective sites, and M denotes the number of X lattice sites.

The key to finding exact solutions is the method of destructive interference. The idea is that an eigenstate of the full Hamiltonian can exhibit zero amplitude on all Y-sites through destructive interference from the X-sites. Let the wave-function of the internal degrees of freedom for the X-site in unit-cell m be denoted by ψ_m, with components $\psi_{m,j}$ where $j = 1, \dots, n$. Destructive interference for the bulk states gives the condition

$$(h^\dagger_{U;+})\psi_m + (h^\dagger_{O;-})\psi_{m+1} = 0, \tag{2.2}$$

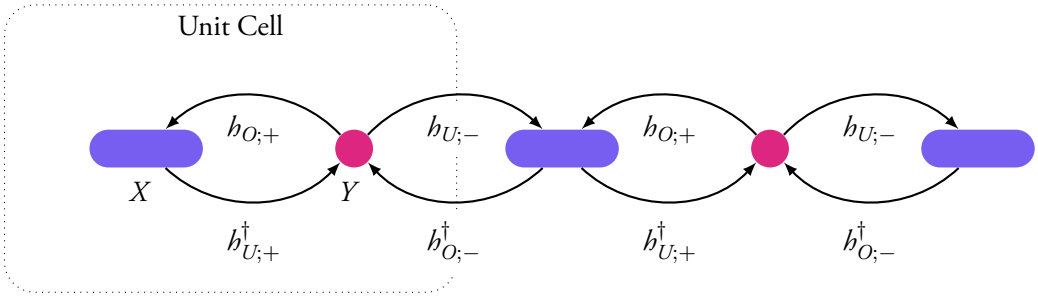

Figure 2.1: The $M = 3$ XY-lattice.

where the comprehensive bulk equations from Equation 2.1 have been simplified using the lack of support from Y-sites. Further, the open boundaries provide the two equations

$$(h_X)\psi_1 = E\psi_1,$$
$$(h_X)\psi_M = E\psi_M.$$

Here, E is the eigenvalue associated with our eigenstate, suggesting that ψ_m should be eigenstates of h_X. To proceed, we make the ansatz of a normalized eigenstate of the form

$$|\Psi_i\rangle = \mathcal{N}_i \sum_{m=1}^{M} r_i^m \left(\sum_{j=1}^{n} c^\dagger_{X_i,m} \phi_{i,j} \right) |0\rangle \,. \tag{2.3}$$

where ϕ_i are the normalized eigenstates of h_X, meaning $i = 1, \ldots, n$. The normalization constant $\mathcal{N}_i$ is given by

$$\mathcal{N}_i = \frac{1}{|r_i|} \sqrt{\frac{|r_i|^2 - 1}{(|r_i|^2)^M - 1}}. \tag{2.4}$$

All ψ_m are thereby assumed to be multiples of ϕ_i, with a relative weight determined by r_i^m. Using this ansatz, Equation 2.2 becomes

$$(h^\dagger_{U;+})\phi_i + r_i(h^\dagger_{O;-})\phi_i = 0, \quad i = 1, \ldots, n,$$

which implies that

$$r_i = -\frac{(h^\dagger_{U;+})\phi_i}{(h^\dagger_{O;-})\phi_i}. \tag{2.5}$$

The value of r_i determines the localization of the state in Equation 2.3. Specifically, $|r_i| < 1$ localizes on the left boundary, $|r_i| = 1$ provides a delocalized state, and $|r_i| > 1$ localizes on the right. This quantity will be referred to as the localization parameter (LP).

While this solution is only exact for the lattice described above, it also becomes a good approximation for the case where an additional Y site is added to the right end, as long as M is large. Under this new boundary condition, complete destructive interference does not generally occur on the right end. After applying the Hamiltonian, the amplitude on the last lattice site of the resultant state is given by $(h^\dagger_{R;+})\psi_M$. From Equation 2.3, this is proportional to $r_i^M \phi_i$. Granted that $|r_i| < 1$, a state of the form described in the ansatz thereby becomes an exact eigenstate in the thermodynamic limit $M \to \infty$.

Finding the left eigenstates is also of relevance in the non-Hermitian context, as these may now be different

from the right. The adjoint Hamiltonian is given by

$$\mathcal{H}_M^\dagger = \begin{pmatrix} h_X^\dagger & h_{U;+} & 0 & 0 & 0 \\ h_{O;+}^\dagger & h_Y^* & h_{U;-}^\dagger & 0 & 0 \\ 0 & h_{O;-} & h_X^\dagger & \dots & 0 \\ 0 & 0 & \vdots & \ddots & h_{U;-} \\ 0 & 0 & 0 & h_{O;-} & h_X^\dagger \end{pmatrix}.$$

The effect on Y sites is mere conjugation since these have a single DOF. Labeling the eigenstates of $h_X^\dagger$ by φ_i, the method of destructive interference provides the eigenstates of the form

$$|\Psi_{L,i}\rangle = \mathcal{N}_{L,i} \sum_{m=1}^{M} r_{L,i}^m \left(\sum_{j=1}^{n} c_{X_i,m}^\dagger \varphi_{i,j} \right) |0\rangle \,, \tag{2.6}$$

with

$$r_{L,i} = -\frac{(h_{O;+}^\dagger)\phi_i}{(h_{U;-}^\dagger)\phi_i}, \quad i = 1, \dots, n. \tag{2.7}$$

The subscript L in $\Psi_{L,i}$, $\mathcal{N}_{L,i}$ and $r_{L,i}$ distinguishes the left eigenstates from the right, and O/U refers to the couplings illustrated in Figure 2.1.

2.3 Biorthogonal quantum mechanics

The framework

Standard quantum mechanics states that once a measurement is made - that is, once the wave-function collapses into an eigenstate of the observable's operator - there are no transitions into other states. If an operator commutes with the Hamiltonian, its eigenstates are called stationary [28], and the collapsed state will remain of definite energy with zero transition probability unless it decoheres. If an operator does not commute with the Hamiltonian, the statement is nevertheless instantaneously true, although time evolution can cause non-zero transition probabilities. The vanishing transition probability is captured by the orthogonality of eigenstates with different eigenvalues. Non-Hermitian operators, however, do not generally have the property that two eigenvectors that correspond to different eigenvalues are orthogonal. Therefore, treating non-Hermitian systems in the same manner as Hermitian ones leads to inconsistencies. Without the orthogonality of eigenstates, non-zero transition probabilities are possible for eigenstates with distinct eigenvalues.

To resolve this inconsistency, biorthogonal quantum mechanics (BQM) has been proposed. The idea stems from the fact that non-Hermitian matrices have biorthogonality, meaning that a right- and a left-eigenvector corresponding to different eigenvalues are orthogonal. We define a right- and left-eigenvector of A by

$$A\,|\phi_i\rangle = \lambda_i\,|\phi_i\rangle\,, \quad \langle\psi_i|\,A = \lambda_i\,\langle\psi_i|\,,$$

respectively. That they share the same set of eigenvalues follows from the fact that we can write

$$(\langle\psi_i|\,A)^T = A^T K|\psi_i\rangle = \lambda_i K|\psi_i\rangle\,,$$

where K is the previously mentioned complex conjugation operator. This is an eigenvalue problem that will, by the invariance of the determinant under transposition, yield the same characteristic polynomial as the right eigenvalue problem for A. With shared eigenvalues in place, the proof of biorthogonality is simple: given a non-Hermitian matrix A with left and right eigenvalues as delineated above, we select $|\phi_1\rangle$ and $|\psi_2\rangle$ with distinct eigenvalues, λ_1 and λ_2. We may then write

$$\langle\psi_1|A|\phi_2\rangle = \langle\psi_1|\lambda_2\phi_2\rangle = \lambda_2\,\langle\psi_1|\phi_2\rangle\,.$$

At the same time,

$$\langle\psi_1|A|\phi_2\rangle = \langle\lambda_1\psi_1|\phi_2\rangle = \lambda_1 \langle\psi_1|\phi_2\rangle .$$

Consequently, $(\lambda_2 - \lambda_1)\langle\psi_1|\phi_2\rangle = 0$ and since $\lambda_1 \neq \lambda_2$ it follows that $|\psi_1\rangle$ and $|\phi_2\rangle$ must be orthogonal.

The transition probability between two normalized states $|a\rangle$ and $|b\rangle$ is given by $P = |\langle a|b\rangle|^2$. BQM proposes a redefinition of the inner product, which combines left and right eigenstates. Specifically, Brody [29] describes how one can define associated states

$$|\psi\rangle = \sum_n c_n |\phi_{R,n}\rangle , \quad \langle\tilde{\psi}| = \sum_n c_n^* \langle\phi_{L,n}| .$$

Here, the sets formed by $|\phi_{R,n}\rangle$ and $|\phi_{L,n}\rangle$ for the permitted values of n are the eigenbases of A and $A^\dagger$ respectively. Given two states

$$|\psi\rangle = \sum_n c_n |\phi_{R,n}\rangle \quad \text{and} \quad |\varphi\rangle = \sum_n d_n |\phi_{R,n}\rangle ,$$

the inner product is defined as

$$\langle\varphi,\psi\rangle \equiv \langle\tilde{\varphi}|\psi\rangle = \sum_{n,m} d_n^* c_m \langle\phi_{L,n}|\phi_{R,m}\rangle. \tag{2.8}$$

Equation 2.8 may be simplified using the widely adopted norm convention

$$\langle\phi_{L,n}|\phi_{R,n}\rangle = 1.$$

Assuming the system is non-degenerate,

$$\begin{aligned}\langle\varphi,\psi\rangle &= \sum_{n,m} d_n^* c_m \delta_{nm} \\ &= \sum_n d_n^* c_n.\end{aligned}$$

Generalizations of other features of standard quantum mechanics can also be found. For example, after proving the linear independence of the eigenstates, Brody arrives at the new completeness relation:

$$\sum_n \frac{|\phi_{L,n}\rangle \langle\phi_{R,n}|}{\langle\phi_{L,n}|\phi_{R,n}\rangle} = I,$$

where I is the identity operator. The equation can be simplified using the previously introduced norm convention, such that

$$\sum_n |\phi_{L,n}\rangle \langle\phi_{R,n}| = I.$$

A matrix representation of a non-Hermitian operator can be defined through the biorthogonal basis $\{|\phi_{L,n}\rangle , |\phi_{R,n}\rangle\}$ [29], [30]. We may quickly identify the matrix components as A_{ij} in

$$A = \left(\sum_i |\phi_{L,i}\rangle\langle\phi_{R,i}|\right) A \left(\sum_j |\phi_{L,j}\rangle\langle\phi_{R,j}|\right) = \sum_{ij} |\phi_{L,i}\rangle \underbrace{\langle\phi_{L,i}|A|\phi_{R,j}\rangle}_{A_{ij}} \langle\phi_{R,j}|.$$

However, while the Hamiltonians considered in the context of this thesis will generally be non-Hermitian, the position and momentum operator both remain Hermitian. Consequently, the biorthogonal framework has no impact on the representation in the eigenstates of these operators. Of high relevance to this thesis, however, is the expectation value, which sees a similar redefinition. For a state $|\psi\rangle = \sum_n c_n |\phi_{R,n}\rangle$,

$$\langle A\rangle = \frac{\langle\tilde{\psi}|A|\psi\rangle}{\langle\tilde{\psi}|\psi\rangle}.$$

Finally, we draw attention to the fact that all new definitions simplify into standard quantum mechanics when Hermiticity is present.

Biorthogonal polarization

It will be illustrated that the bulk-boundary correspondence (BBC) may be broken in non-Hermitian systems. The two standard methods to restore it are the generalized Brillouin zone and biorthogonal BBC [8]. The former suggests that the wave-functions for the non-Hermitian lattice are not Bloch waves; instead, they are non-Bloch waves, given by re^{-ikx} [31]. The biorthogonal BBC approach, on the other hand, will be the focus of this thesis. Briefly summarized, it argues that transition points between topological phases correspond to the delocalization of biorthogonal boundary states [32]. The delocalization is described by the biorthogonal expectation value of the projection operator

$$\Pi_m = \sum_\alpha c^\dagger_{m,\alpha} c_{m,\alpha},$$

where $c^\dagger_{m,\alpha}$ and $c_{m,\alpha}$ denote the creation and annihilation operators for site α in unit cell m. For eigenstates $|\psi_L\rangle$ and $|\psi_R\rangle$ as derived for the *XY*-lattice, with the internal DOF representing lattice sites, the localization is given by

$$\langle\psi_L|\Pi_m|\psi_R\rangle = \mathcal{N}_L^*\mathcal{N}_R\,(r_L^* r_R)^m \left(\sum_{ij}^{m} \varphi_i^*\phi_j\, c_{m,\alpha_i} c^\dagger_{m,\alpha_j}\right) = \mathcal{N}_L^*\mathcal{N}_R\,(r_L^* r_R)^m,$$

where the biorthogonality and normalization of φ and ϕ, the left and right eigenstates of the *X*-site Hamiltonian, was used. An exact bulk state is found when $|r_L^* r_R| = 1$. The quantity called the biorthogonal polarization [32] is defined as

$$P = 1 - \lim_{M\to\infty} \left\langle \psi_L \left| \frac{\sum m\Pi_m}{M} \right| \psi_R \right\rangle. \tag{2.9}$$

The biorthogonal polarization exhibits an integer jump at the point where the boundary state becomes delocalized. Specifically, it takes on the value 0 for a state localized on the right boundary and 1 for a state localized on the left. It thereby constitutes a topological invariant that predicts the boundary states of the system, restoring the BBC. We note that in the biorthogonal framework, the normalization presented in Equation 2.4 must be redefined using the biorthogonal expectation value. The result is given by

$$\mathcal{N}_L^*\mathcal{N}_R = \frac{1}{r_L^* r_R} \cdot \frac{r_L^* r_R - 1}{(r_L^* r_R)^M - 1}. \tag{2.10}$$

2.4 The Su-Schrieffer-Heeger model

The Su-Schrieffer-Heeger model is the simplest paradigmatic example of topological insulators. Originally introduced as a model of polyacetylene [33], it describes a one-dimensional lattice consisting of two sites, *A* and *B*, per unit cell. The lattice is illustrated in Figure 2.2. Couplings between sites are restricted to the nearest neighbors, and no on-site potentials are considered. The Hermitian Hamiltonian is thereby written in terms of two hopping parameters, t_1 and t_2. Non-hermiticity may be introduced in various ways, but in this thesis, attention will be focused on the anisotropic version. In this case, the Hamiltonian is given by

$$H = \sum_{m=1}^{M} \left[(t_1+\gamma)c^\dagger_{m,A}\, c_{m,B} + (t_1-\gamma)c^\dagger_{m,B}\, c_{m,A}\right] + \sum_{m=1}^{M-1} \left(t_2 c^\dagger_{m,A}\, c_{m+1,B} + h.c.\right). \tag{2.11}$$

Here, *h.c.* represents the Hermitian conjugate of the preceding term. Real hopping amplitudes are assumed, $t_1, t_2, \gamma \in \mathbb{R}$. When represented as a matrix in the lattice-site basis, the Hamiltonian takes the form

$$\begin{bmatrix} 0 & t_1+\gamma & 0 & 0 & \dots \\ t_1-\gamma & 0 & t_2 & 0 & \dots \\ 0 & t_2 & 0 & t_1+\gamma & \dots \\ 0 & 0 & t_1-\gamma & 0 & \dots \\ \vdots & \vdots & \vdots & \vdots & \ddots \end{bmatrix}.$$

For a long lattice chain, each end of the lattice can be locally mapped onto the *XY*-lattice. For the left end,

$$\begin{aligned} h_X &= 0, \\ h_Y &= 0, \\ h_{O;+} &= t_1 + \gamma, \\ h_{U;+} &= t_1 - \gamma, \\ h_{O/U;-} &= t_2. \end{aligned}$$

This mapping means that the left boundary state only lives on the *A*-sites, with energy 0. The LPs, as per Equation 2.5 and Equation 2.7, are given by

$$r_R = -\frac{t_1 - \gamma}{t_2}, \quad r_L = -\frac{t_1 + \gamma}{t_2},$$

and the biorthogonal bulk condition predicts phase transition points at $|r_L^* r_R| = \left|\frac{t_1^2 - \gamma^2}{t_2^2}\right| = 1$. The derivation for the right end is exactly analogous, but with the wave-function finding support only on *B*-sites. In this case,

$$r_R = -\frac{t_2}{t_1 + \gamma}, \quad r_L = -\frac{t_2}{t_1 - \gamma}.$$

The transition points are thereby the same as for the left end. While neither boundary state is exact for this system, they are good approximations for long lattices and highlight the flexibility of the *XY*-lattice model solutions.

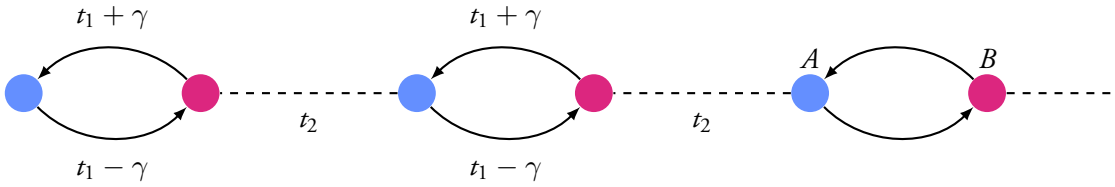

Figure 2.2: The NH SSH chain.

When transformed into a plane-wave basis, Equation 2.11 simplifies to the so-called Bloch Hamiltonian,

$$H(k) = \begin{pmatrix} 0 & t_1 + \gamma + t_2 e^{-ik} \\ t_1 - \gamma + t_2 e^{ik} & 0 \end{pmatrix}.$$

An analysis of the Bloch Hamiltonian reveals TRS, SLS, and PHS. The presence of SLS, which manifests as anti-commutation with the Pauli matrix σ_z, permits a winding number to be defined. However, such topological invariants fail to predict boundary states under open boundary conditions (OBC) [8], meaning conventional BBC is broken; this is demonstrated in Figure 2.3 using a common winding number that when adapted to the NH SSH chain is defined by

$$\nu = \frac{1}{2\pi} \int_{-\pi}^{\pi} \frac{t_2 \left(i\gamma \sin(k) + t_1 \cos(k) + t_2\right)}{\gamma^2 + t_1^2 + 2t_1 t_2 \cos(k) + t_2^2} dk.$$

A 2×2 Bloch Hamiltonian can be expressed as $H(k) = h(k) \cdot \vec{\sigma}$, where $\vec{\sigma}$ is the vector of Pauli matrices. The winding number can then also be written as $\nu = \frac{1}{2}(\nu_1 + \nu_2)$, where ν_1 and ν_2 are integer winding numbers defined by how the vector $h(k)$ winds around the two respective EPs [34]. The winding number ν consequently takes half-integer values.

In Figure 2.3, the boundary states can be observed as the zero energy eigenvalue under OBC. They appear at noticeably different energies than the phase transitions predicted by the winding number. We note that the winding number transitions instead coincide with gap closings under periodic boundary conditions (PBC). The biorthogonal bulk condition, on the other hand, accurately predicts the boundary states, as seen by the vertical dashed lines.

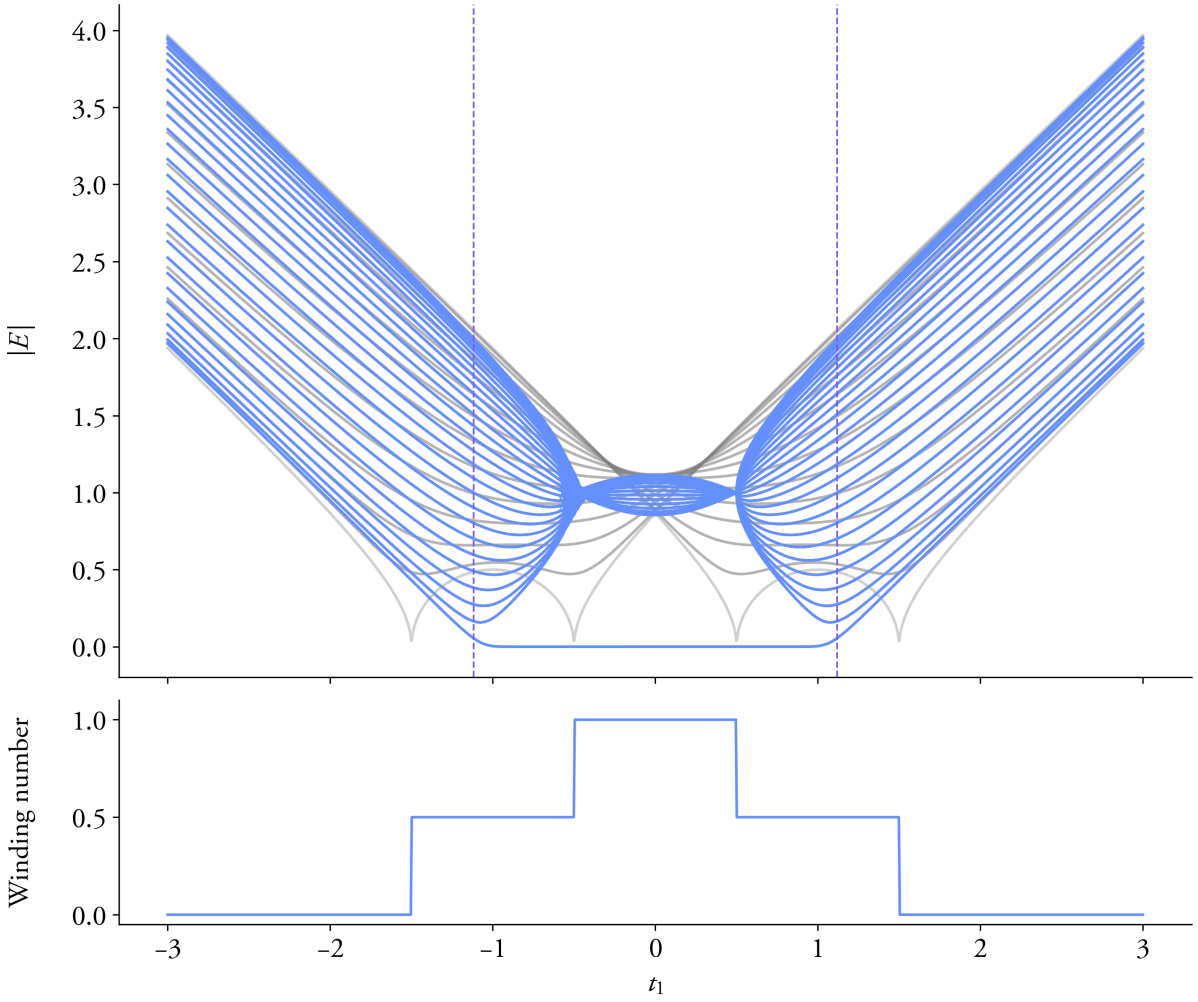

Figure 2.3: The broken BBC for the NH SSH chain. The upper panel shows the absolute value of the energy spectrum, where the blue lines are under open boundary conditions and the gray lines are under periodic boundary conditions. Vertical dashed lines show the biorthogonal transition points. The lower panel shows the winding number. The panels share the same x-axis and were evaluated at $t_1 = 1$ and $\gamma = 0.5$.

3 Results

3.1 Model

The trimer SSH chain extends on the SSH model by introducing an extra lattice site to each unit cell. The lattice sites will be denoted by A, B, and C. With three sites, there are three hopping amplitudes, t_1, t_2, and t_3, assigned as illustrated in Figure 3.1. In order to explore non-Hermitian effects, the anisotropic γ-term between sites A and B is retained from the standard SSH chain. From now on, SSH3 will refer to this anisotropic model.

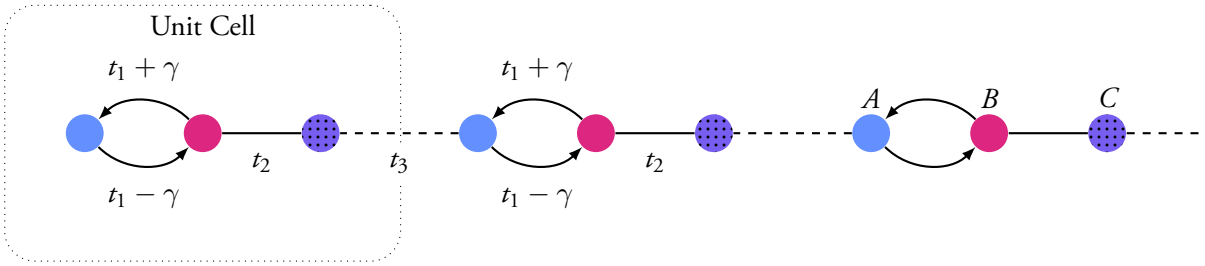

Figure 3.1: The SSH3 chain.

The Hamiltonian of the SSH3 chain with M unit cells is given by

$$H = \sum_{m=1}^{M} \left[(t_1+\gamma) c_{m,A}^{\dagger} c_{m,B} + (t_1-\gamma) c_{m,B}^{\dagger} c_{m,A} \right] + \sum_{m=1}^{M} \left(t_2 c_{m,B}^{\dagger} c_{m,C} + h.c. \right) + \sum_{m=1}^{M-1} \left(t_3 c_{m,A}^{\dagger} c_{m+1,C} + h.c. \right).$$

Alternatively, it may be presented in matrix form, with the spatial states as a basis:

$$\begin{bmatrix} 0 & t_1+\gamma & 0 & 0 & 0 & 0 & \dots \\ t_1-\gamma & 0 & t_2 & 0 & 0 & 0 & \dots \\ 0 & t_2 & 0 & t_3 & 0 & 0 & \dots \\ 0 & 0 & t_3 & 0 & t_1+\gamma & 0 & \dots \\ 0 & 0 & 0 & t_1-\gamma & 0 & t_2 & \dots \\ 0 & 0 & 0 & 0 & t_2 & 0 & \dots \\ \vdots & \vdots & \vdots & \vdots & \vdots & \vdots & \ddots \end{bmatrix}.$$

Three forms of the lattice will be examined, corresponding to three different boundary conditions for the right end. The left end is assumed to always start with an A-site. The three cases will be labeled according to the total number of lattice sites they host: $3M-1$, $3M$, and $3M+1$.

Following Asbóth [35], a plane-wave basis is introduced for the external DOF:

$$|k\rangle = \frac{1}{\sqrt{M}} \sum_{m=1}^{M} e^{imk} |m\rangle, \quad k = \frac{2\pi j}{M} \text{ for } j \in \{1, 2, \dots, M\},$$

where M is the total number of unit cells, $|m\rangle$ are the basis states for the external DOF, and k is the wavenumber. With the new basis, the bulk momentum-space Hamiltonian is defined as $\langle k|H|k\rangle$. Through matrix

manipulation presented in Appendix A, the bulk Hamiltonian simplifies to the Bloch Hamiltonian,

$$H(k) = \begin{pmatrix} 0 & t_1 + \gamma & t_3 e^{-ik} \\ t_1 - \gamma & 0 & t_2 \\ t_3 e^{ik} & t_2 & 0 \end{pmatrix}. \tag{3.1}$$

Explicitly, the full Hamiltonian is given by $H = \bigoplus_k H(k)$. Given eigenstates $|u_n(k)\rangle$ of $H(k)$, the complete eigenstate of the Hamiltonian is given by the tensor product $|\Psi_n(k)\rangle = |k\rangle \otimes |u_n(k)\rangle$.

3.2 Symmetries

Characterizing the spectrum of the Bloch Hamiltonian is simplified by an investigation into its symmetries. Among the symmetries in Table 2.1, the NH SSH3 model only possesses TRS. The matrix $H^*(-k)$ is obtained from H by complex conjugation, followed by the reversal of signs for k: two operations that each reverse the sign of the exponents in the hopping terms, leaving the Hamiltonian unaltered. The operator T in the symmetry constraint is thereby the identity operator and the energy constraint is satisfied for the entire parameter space.

Because the Bloch Hamiltonian is a 3×3 matrix, SLS is generally not possible. Reversing the sign through a unitary transformation generally requires an even number of sites. For the SSH6, the SSH variant with six lattice sites per unit cell, SLS is present and given by $S = \bigoplus_{m=1}^{3} \sigma_z$, where σ_z is the third Pauli matrix. However, due to SLS in the SSH6, the SSH3 has a related symmetry that has been labeled point chiral symmetry [36]. The symmetry constraint is

$$SH(k)S^{-1} = -H(\pi + k), \tag{3.2}$$

with $S = \mathrm{diag}(1, -1, 1)$. The symmetry can be seen from

$$\begin{pmatrix} 1 & 0 & 0 \\ 0 & -1 & 0 \\ 0 & 0 & 1 \end{pmatrix} \begin{pmatrix} 0 & t_1 + \gamma & t_3 e^{-ik} \\ t_1 - \gamma & 0 & t_2 \\ t_3 e^{ik} & t_2 & 0 \end{pmatrix} \begin{pmatrix} 1 & 0 & 0 \\ 0 & -1 & 0 \\ 0 & 0 & 1 \end{pmatrix} = \begin{pmatrix} 0 & -t_1 - \gamma & t_3 e^{-ik} \\ \gamma - t_1 & 0 & -t_2 \\ t_3 e^{ik} & -t_2 & 0 \end{pmatrix}.$$

As the introduction of an extra π phase is the same as multiplying the t_3 elements by -1, the expression above is equivalent to $-H(\pi + k)$. This introduces the energy constraint $\{\varepsilon(k)\} = \{-\varepsilon(\pi + k)\}$.

PHS is also absent in SSH3, although in the same vein as CS, a point particle-hole symmetry may be defined as

$$CH(k)C^{-1} = -H^*(\pi - k).$$

The operator C is given by $C = \mathrm{diag}(1, -1, 1)$, and the energy constraint becomes $\{\varepsilon(k)\} = \{-\varepsilon^*(\pi - k)\}$.

3.3 The Hermitian case

Before treating the anisotropic version, the Hermitian SSH3 model will be considered. Without chiral symmetry, it is not possible to define a winding number for the SSH3 model in the same way as for the SSH model. However, through what Anastasiadis et al. [36] refer to as normalized sublattice Zak's phase, it is nevertheless possible to establish a bulk-boundary correspondence. For $3M$ sites, the same study determined that the transition points between topological phases are found at $t_3 = \pm t_1$ and $t_3 = \pm t_2$. The localized boundary states are visualized in Figure 3.2 together with the OBC spectrum and the transition points. The transitions are not generally associated with the gap closing, as can be seen from the energy spectrum in the inset. In the case of $3M + 1$ lattice sites, Anastasiadis et al. found that transitions instead occur at $t_2 = \pm t_3$ and $t_2 = \pm t_1$. Finally, for $3M - 1$ sites, their approach predicts a constant number of edge states for the entire parameter space and does not mark any transition points.

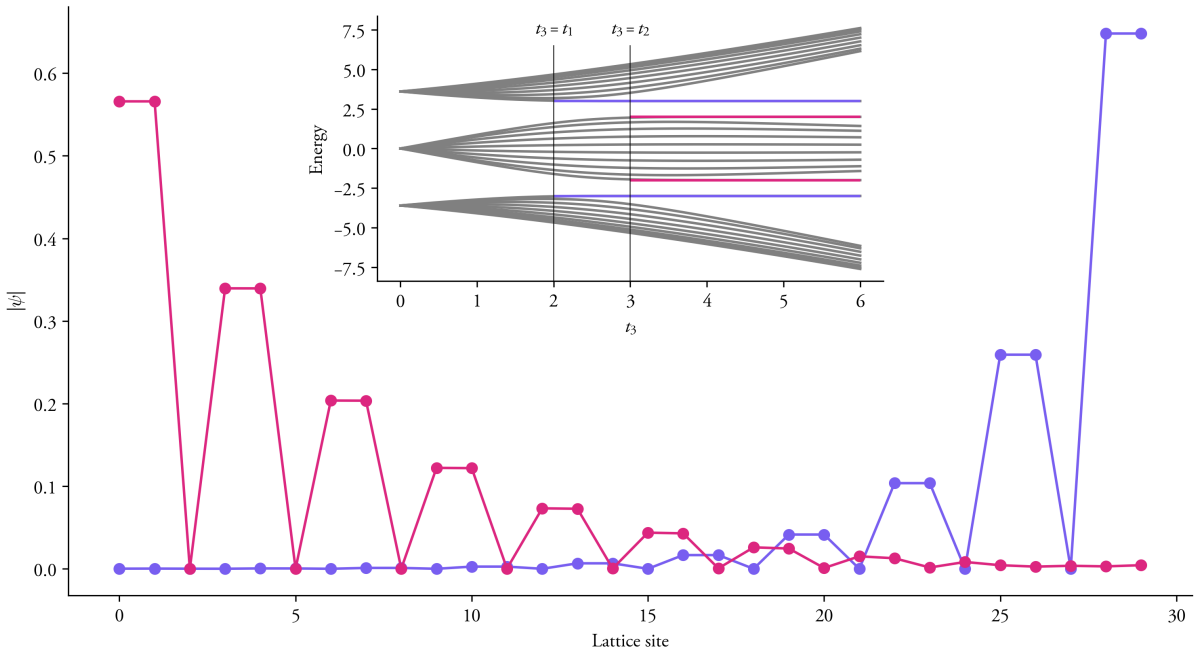

Figure 3.2: The spatial profile of the boundary states for the Hermitian SSH3 model, defined by the absolute value of the lattice-site amplitudes. The inset shows the OBC energy spectrum. The transition points are marked in the energy plot with vertical lines. The plot uses $t_1 = 2$, $t_2 = 3$, and $N = 30$, with the spatial profiles being evaluated at $t_3 = 5$.

3.4 Boundary states

In section 3.4, the *XY*-lattice with its exactly solvable boundary conditions was introduced. The Hamiltonian for this lattice was given by Equation 2.1. In the current section, the SSH3 model is mapped to the *XY*-lattice to find the boundary states. The three cases, $3M-1$, $3M$, and $3M+1$, are considered separately. Due to the similarities of the latter two cases, the $3M+1$ case has been placed in Appendix B.

Boundaries for $3M-1$ sites

With $3M-1$ sites, the SSH3 starts with an *A*-site and ends in a *B*-site. By drawing an equivalence between *C* and *Y*, and letting the internal DOF of the *X*-sites represent sites *A* and *B*, the SSH3 is exactly described by the *XY*-lattice. The hopping terms in Equation 2.1 are thereby given by

$$\begin{aligned} h_X &= \begin{pmatrix} 0 & t_1+\gamma \\ t_1-\gamma & 0 \end{pmatrix}, \\ h_Y &= 0, \\ h^\dagger_{O/U;+} &= \begin{pmatrix} 0 & t_2 \end{pmatrix}, \\ h^\dagger_{O/U;-} &= \begin{pmatrix} t_3 & 0 \end{pmatrix}. \end{aligned}$$

Starting with the right eigenstates, the ansatz in Equation 2.3 is applied:

$$|\Psi_i\rangle = \mathcal{N}_i \sum_{m=1}^{M} r_i^m \left(\sum_{j=1}^{n} c^\dagger_{X_i,m} \phi_{i,j} \right) |0\rangle .$$

The states ϕ_i are the eigenstates of h_X, given by

$$\phi_1 = \begin{pmatrix} \sqrt{\frac{t_1+\gamma}{2t_1}} \\ -\sqrt{\frac{t_1-\gamma}{2t_1}} \end{pmatrix}, \quad \phi_2 = \begin{pmatrix} \sqrt{\frac{t_1+\gamma}{2t_1}} \\ \sqrt{\frac{t_1-\gamma}{2t_1}} \end{pmatrix},$$

and corresponding to eigenvalues $E = -\sqrt{t_1^2 - \gamma^2}$ and $E = \sqrt{t_1^2 - \gamma^2}$, respectively. The localization parameter, r_i, is given by Equation 2.5, providing the solutions

$$r_1 = \frac{t_2\sqrt{t_1 - \gamma}}{t_3\sqrt{t_1 + \gamma}}$$
$$r_2 = -\frac{t_2\sqrt{t_1 - \gamma}}{t_3\sqrt{t_1 + \gamma}}.$$

Hence, we have the full wave-functions:

$$|\Psi_{R,1}\rangle = \mathcal{N}_{R,1} \sum_{m=1}^{M} \left(\frac{t_2\sqrt{t_1 - \gamma}}{t_3\sqrt{t_1 + \gamma}}\right)^m \left(\sqrt{\frac{t_1+\gamma}{2t_1}} c_{A,m}^\dagger - \sqrt{\frac{t_1-\gamma}{2t_1}} c_{B,m}^\dagger\right) |0\rangle$$
$$|\Psi_{R,2}\rangle = \mathcal{N}_{R,2} \sum_{m=1}^{M} \left(-\frac{t_2\sqrt{t_1 - \gamma}}{t_3\sqrt{t_1 + \gamma}}\right)^m \left(\sqrt{\frac{t_1+\gamma}{2t_1}} c_{A,m}^\dagger + \sqrt{\frac{t_1-\gamma}{2t_1}} c_{B,m}^\dagger\right) |0\rangle$$

The left-eigenvectors corresponding to the same eigenvalues are found by the same procedure, but starting with the adjoint Hamiltonian $H_M^\dagger$. This matrix differs from $\mathcal{H}_M$ only in that h_X is replaced by $h_X^\dagger$. The eigenvectors of $h_X^\dagger$ are given by

$$\phi_1 = \begin{pmatrix} \sqrt{\frac{t_1-\gamma}{2t_1}} \\ -\sqrt{\frac{t_1+\gamma}{2t_1}} \end{pmatrix}, \quad \phi_2 = \begin{pmatrix} \sqrt{\frac{t_1-\gamma}{2t_1}} \\ \sqrt{\frac{t_1+\gamma}{2t_1}} \end{pmatrix},$$

and correspond to $E = -\sqrt{t_1^2 - \gamma^2}$ and $E = \sqrt{t_1^2 - \gamma^2}$, respectively. The solutions of r_i are then given by

$$r_{L,1} = \frac{t_2\sqrt{t_1 + \gamma}}{t_3\sqrt{t_1 - \gamma}}$$
$$r_{L,2} = -\frac{t_2\sqrt{t_1 + \gamma}}{t_3\sqrt{t_1 - \gamma}}.$$

Finally, the left eigenstates can be written as

$$|\Psi_{L,1}\rangle_L = \mathcal{N}_{L,1} \sum_{m=1}^{M} \left(\frac{t_2\sqrt{t_1 + \gamma}}{t_3\sqrt{t_1 - \gamma}}\right)^m \left(\sqrt{\frac{t_1-\gamma}{2t_1}} c_{A,m}^\dagger - \sqrt{\frac{t_1+\gamma}{2t_1}} c_{B,m}^\dagger\right) |0\rangle ,$$
$$|\Psi_{L,2}\rangle = \mathcal{N}_{L,2} \sum_{m=1}^{M} \left(-\frac{t_2\sqrt{t_1 + \gamma}}{t_3\sqrt{t_1 - \gamma}}\right)^m \left(\sqrt{\frac{t_1-\gamma}{2t_1}} c_{A,m}^\dagger + \sqrt{\frac{t_1+\gamma}{2t_1}} c_{B,m}^\dagger\right) |0\rangle .$$

As with the *XY*-lattice, these boundary states are valid on either end of the SSH3 chain, and the localization depends on the magnitude of their corresponding r-value. The condition for a biorthogonal bulk state is $|r_{L,i}^* r_{R,i}| = 1$. For the eigenstates above,

$$|r_{L,1}^* r_{R,1}| = |r_{L,2}^* r_{R,2}| = \left|\frac{t_2\sqrt{t_1 + \gamma}}{t_3\sqrt{t_1 - \gamma}} \cdot \frac{t_2\sqrt{t_1 - \gamma}}{t_3\sqrt{t_1 + \gamma}}\right| = \frac{t_2^2}{t_3^2}.$$

It follows that the expected transition points occur at $t_2 = \pm t_3$.

Boundaries for $3M$ sites

With $3M$ sites, the SSH3 starts with an A-site and ends with a C-site. The left end locally maps to the above case, and the eigenstates found there are consequently also valid approximations here, provided the chain is sufficiently long and the $r_{L/R,i}$ parameters cause the localization of their corresponding states on the left boundary. The right end, however, must be treated separately. In order to make the XY-lattice description valid for the right boundary, its hopping terms are given by

$$\begin{aligned} h_X &= \begin{pmatrix} 0 & t_2 \\ t_2 & 0 \end{pmatrix}, \\ h_Y &= 0, \\ h^\dagger_{O/U;+} &= \begin{pmatrix} 0 & t_3 \end{pmatrix}, \\ h^\dagger_{O;-} &= \begin{pmatrix} t_1+\gamma & 0 \end{pmatrix}, \\ h^\dagger_{U;-} &= \begin{pmatrix} t_1-\gamma & 0 \end{pmatrix}. \end{aligned}$$

The eigenvalues of h_X are $E = \pm t_2$, and the eigenstates are given by

$$\phi_{R,1} = \begin{pmatrix} 1 \\ 1 \end{pmatrix}, \quad \phi_{R,2} = \begin{pmatrix} 1 \\ -1 \end{pmatrix}.$$

The localization parameters are

$$\begin{aligned} r_{R,1} &= -\frac{t_3}{t_1+\gamma}, \quad r_{R,2} = \frac{t_3}{t_1+\gamma}, \\ r_{L,1} &= -\frac{t_3}{t_1-\gamma}, \quad r_{L,2} = \frac{t_2}{t_1-\gamma}. \end{aligned}$$

The exact solutions are then

$$\begin{aligned} |\Psi_{R,1}\rangle &= \mathcal{N}_{R,1} \sum_{m=1}^{M} \left(-\frac{t_3}{t_1+\gamma}\right)^m \left(c^\dagger_{A,m} + c^\dagger_{C,m}\right)|0\rangle, \\ |\Psi_{R,2}\rangle &= \mathcal{N}_{R,2} \sum_{m=1}^{M} \left(\frac{t_3}{t_1+\gamma}\right)^m \left(c^\dagger_{A,m} - c^\dagger_{C,m}\right)|0\rangle, \\ |\Psi_{L,1}\rangle &= \mathcal{N}_{L,1} \sum_{m=1}^{M} \left(-\frac{t_3}{t_1-\gamma}\right)^m \left(c^\dagger_{A,m} + c^\dagger_{C,m}\right)|0\rangle, \\ |\Psi_{L,2}\rangle &= \mathcal{N}_{L,2} \sum_{m=1}^{M} \left(\frac{t_3}{t_1-\gamma}\right)^m \left(c^\dagger_{A,m} - c^\dagger_{C,m}\right)|0\rangle. \end{aligned}$$

Finally,

$$\left|r^*_{L,1} r_{R,1}\right| = \left|r^*_{L,2} r_{R,2}\right| = \left|\frac{t_3^2}{t_1^2 - \gamma^2}\right|,$$

and the transition points are expected at $t_3^2 = |t_1^2 - \gamma^2|$. It is worth noting that the above solutions are only exact for the right end in the thermodynamic limit. The same is true for the left end states. However, the biorthogonal bulk condition is still a good approximation when either the left or right state localizes on the wrong end, despite the ansatz not being valid. This follows from how the contribution of the ends to the biorthogonal product goes to zero in the thermodynamic limit when the left and right states are localized on opposite ends. This is the case for the transition points, as can be seen from the LPs and the biorthogonal condition $|r^*_L r_R| = 1$. Consequently, we expect that the biorthogonal transition points are good approximations for the $3M$ case, assuming the chain is sufficiently long. The ansatz, however, will only be valid for either the left or right eigenstate under such conditions.

Zero modes

Point chiral symmetry in a lattice with an odd number of states leads to a zero-energy state. Available literature [16] has shown that the zero-energy states can be distinguished from typical bulk states and the localized boundary states discussed above by their spatial profile. Here, the zero modes are investigated from the perspective of biorthogonal quantum mechanics.

The notation $e_{m,\alpha}$ for $\alpha \in \{A, B, C\}$ is introduced as a shorthand for $c^\dagger_{m,\alpha}|0\rangle$. The bulk conditions for the zero mode are then given by

$$\begin{aligned} t_3 e_{m-1,C} + (t_1 + \gamma) e_{m,B} &= 0 \\ (t_1 - \gamma) e_{m,A} + t_2 e_{m,C} &= 0 \\ t_2 e_{m,B} + t_3 e_{m+1,A} &= 0 \end{aligned}$$

Similarly, the boundary condition of the left end is given by

$$(t_1 + \gamma) e_{1,B} = 0$$

This boundary condition requires $e_{1,B} = 0$, which by the bulk conditions implies that every site located an even number of jumps away from $e_{1,B}$ must also have zero amplitude. This means that all odd sites must have zero amplitude. Further, the amplitude changes by a factor $r_0 = \sqrt{-\frac{t_1+\gamma}{t_1-\gamma}}$ when moving one unit cell to the right. For non-zero γ, it follows that the state will be exponentially localized on one end. We can write this state as

$$|\Psi_0\rangle = \mathcal{N}_0 \sum_{m=1}^{M} r_0^m \left[\delta_{m,\text{odd}} \left(c^\dagger_{A,m} - \frac{t_1 - \gamma}{t_2} c^\dagger_{C,m} \right) - \delta_{m,\text{even}} \frac{t_3}{t_2} r_0 \, c^\dagger_{B,m} \right] |0\rangle$$

with $\mathcal{N}_0$ the normalization constant and $\delta_{m,\text{even/odd}}$ selecting the even or odd unit cells. The possible right boundary conditions are given by

$$\begin{aligned} t_3 e_{M,C} &= 0 \quad \text{for } N = 3M + 1 \\ (t_1 - \gamma) e_{M,A} &= 0 \quad \text{for } N = 3M - 1 \\ t_2 e_{M,B} &= 0 \quad \text{for } N = 3M. \end{aligned}$$

In the case that $r_0 > 1$, one of these becomes the important edge condition in the thermodynamic limit. The only difference, however, is which sites have zero amplitude in which unit cells. There is still a zero amplitude at every other site, such that it satisfies bulk and boundary conditions. This distinct spatial profile is visualized in Figure 3.3(d). An average of the spatial profile of all right eigenstates is presented in the same figure, illustrating the non-Hermitian skin effect. For the zero mode, the product $r_L^* r_R$ ends up being ± 1, depending on whether r_0 is real or imaginary. Therefore, it always satisfies the condition for an exact bulk state and is distinguishable from the topologically protected boundary states through the biorthogonal framework.

Topological invariants

With all cases considered, we turn to the biorthogonal polarization as a potential topological invariant. The results above show that the biorthogonal transition points in certain cases coincide with the Hermitian case. However, this is not generally the case, as observed in the transition points at $t_3 = \pm\sqrt{t_1^2 - \gamma^2}$ for the $3M$ case. A plot of the energy spectrum, along with the biorthogonal polarization, is shown in Figure 3.4. The biorthogonal polarization is calculated as presented in Equation 2.9, using the states outlined above. The boundary state that deviates from the Hermitian transition point is shown in purple. It is observed that the boundary states appear in connection to the points predicted by the biorthogonal framework.

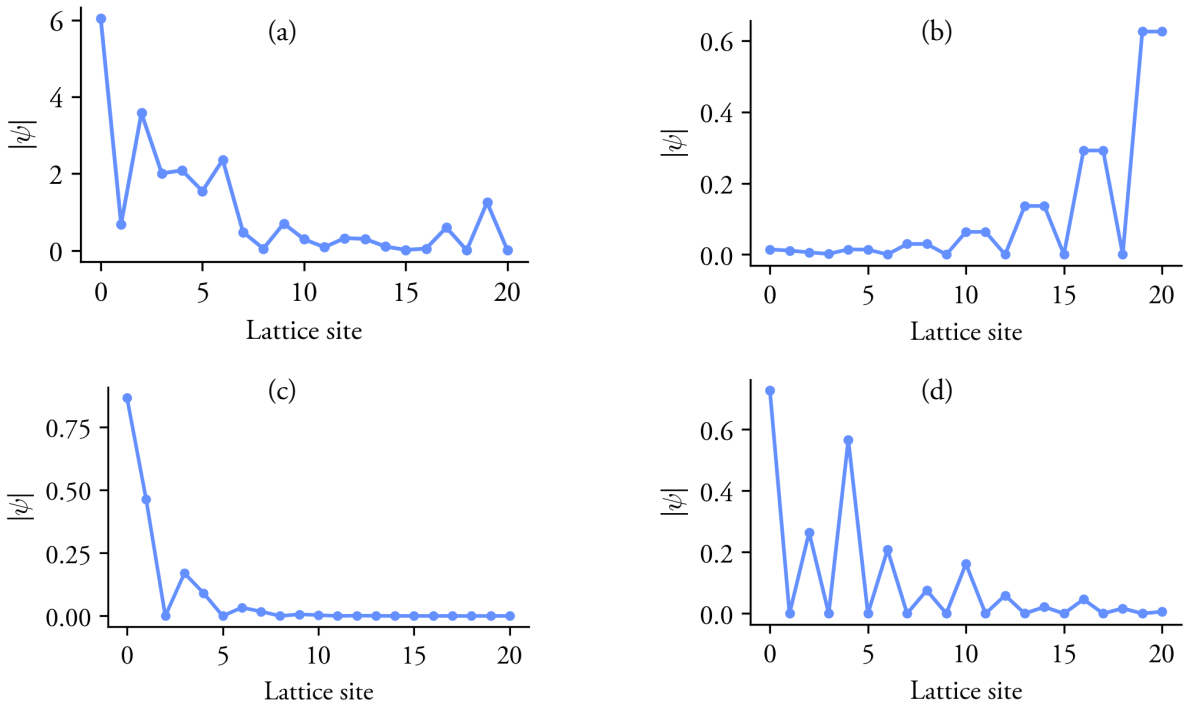

Figure 3.3: The spatial profile of the right eigenstates for the SSH3 model, defined as the absolute value of the lattice-site amplitudes and evaluated at $t_1 = 0.9$, $t_2 = 1.1$, $t_3 = 3$, and $\gamma = 0.5$. (a) The average of all right eigenstates, (b) a boundary state with eigenvalue $\sqrt{t_1^2 - \gamma^2}$, (c) a boundary state with eigenvalue t_2, and (d) a zero mode.

Earlier studies of the anisotropic SSH3 model have suggested a topological invariant defined by Zak's phase [16]. The Zak phase per band is given by

$$\theta_n = -i \int_0^{2\pi} \langle u_{L,n} | \frac{d}{dk} | u_{R,n} \rangle \, dk, \quad n = 1, 2, 3.$$

Here, $|u_{L,n}\rangle$ and $|u_{R,n}\rangle$ are the left and right eigenstates of the nth band of the Bloch Hamiltonian. Unlike the biorthogonal polarization, it is thereby computed for PBC. The proposed topological invariant is the rescaled sum of the Zak phases over all bands [16]:

$$\frac{1}{2\pi} \sum_{n=1}^{3} \theta_n = \begin{cases} 1, & |t_1| \& |t_2| < t_3, \\ 0, & \text{otherwise.} \end{cases}$$

We note that the transitions expected from this invariant do not appear to predict the boundary states. Figure 3.4 thereby illustrates the broken BBC and suggests that the biorthogonal polarization may be a more suitable topological invariant for NH systems with OBC. The same plot for $3M-1$ sites is shown in Figure 3.5. Here, the boundary state solutions are exact, and the biorthogonal polarization again predicts the transition points. The case of $3M+1$ sites is included in Appendix B, and suggests a similar conclusion to the $3M$ case. For all cases, the biorthogonal polarization closely aligns with where the boundary states join the bulk states. The value of P predicts on which end of the lattice the boundary states are localized, with 0 indicating the right end and 1 indicating the left end. For the $3M$ case, the state with eigenvalue $|E| = \sqrt{|t_1^2 - \gamma^2|}$ only exists if localized on the left end, and the $|E| = |t_2|$ state only exists if localized on the right end.

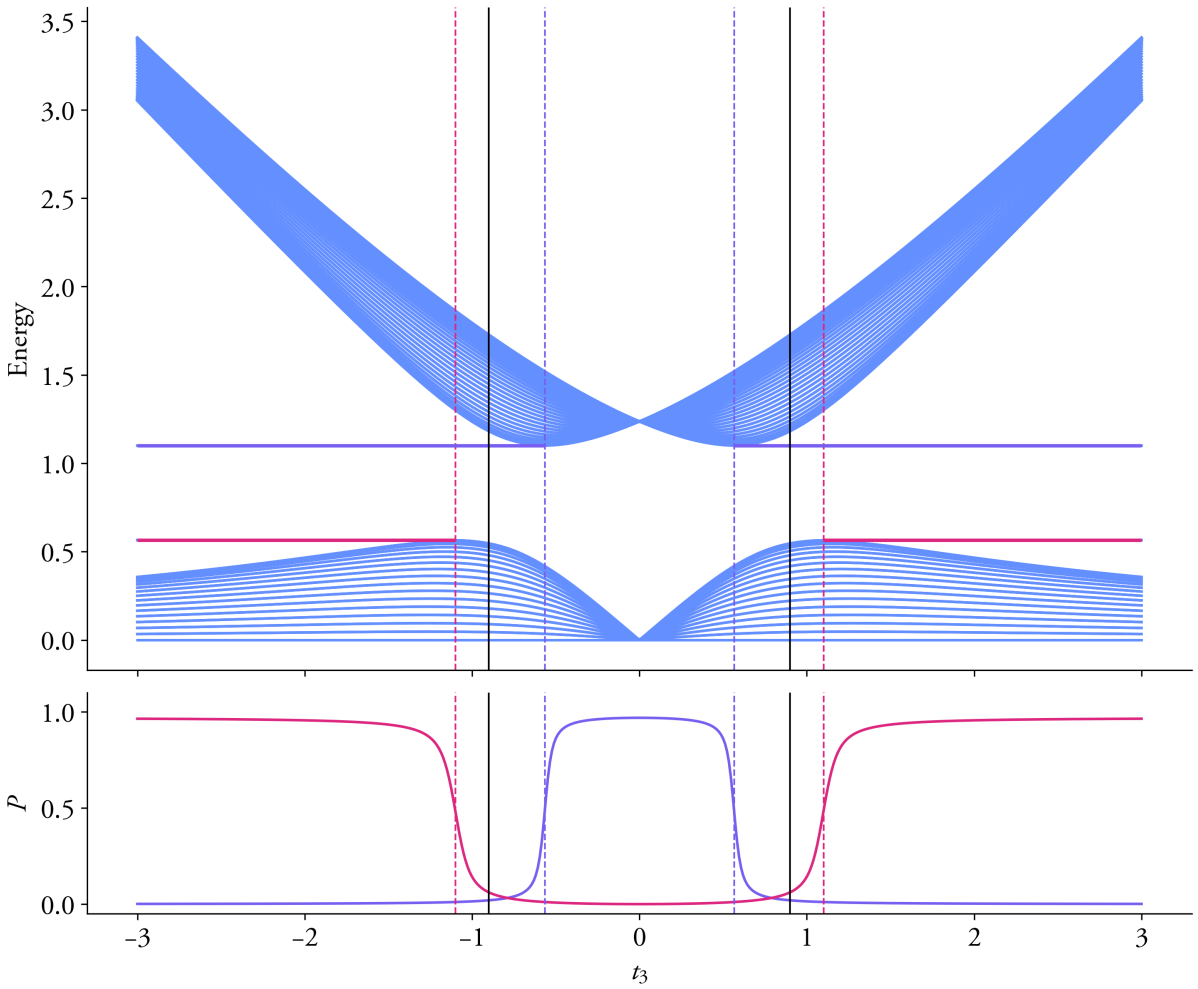

Figure 3.4: The absolute value of the energy spectrum of the SSH3 model of 99 sites, open boundary conditions, and evaluated at $t_1 = 0.9$, $t_2 = 1.1$, $t_3 = 3$, and $\gamma = 0.7$. The biorthogonal transition points are marked with vertical dashed lines. The solid vertical lines show the transition point predicted using Zak's phase. The lower panel shows the biorthogonal polarization of both types of boundary states.

3.5 Exceptional points

For the dimer SSH model, it is possible to characterize phases by a winding number defined in terms of the exceptional points [34]. However, when chiral symmetry is absent, as in the SSH3 model, this procedure cannot be applied. Nevertheless, exceptional points still arise in the SSH3 model and hold significant interest for their potential experimental applications. This section explores all possible exceptional points that can occur in this context.

The eigenvalues of the Bloch Hamiltonian are the solutions E in the determinant problem

$$\begin{vmatrix} -E & t_1+\gamma & t_3e^{-ik} \\ t_1-\gamma & -E & t_2 \\ t_3e^{ik} & t_2 & -E \end{vmatrix} = 0.$$

After expanding out the determinant and collecting similar terms,

$$E^3 - E(t_1^2+t_2^2+t_3^2-\gamma^2) - (t_1+\gamma)t_2t_3e^{ik} - (t_1-\gamma)t_2t_3e^{-ik} = 0. \tag{3.3}$$

The condition for at least one repeated eigenvalue can be phrased in terms of the discriminant of the characteristic polynomial. In Equation 3.3, the polynomial is in the form of a depressed cubic, $x^3 + px + q$. We

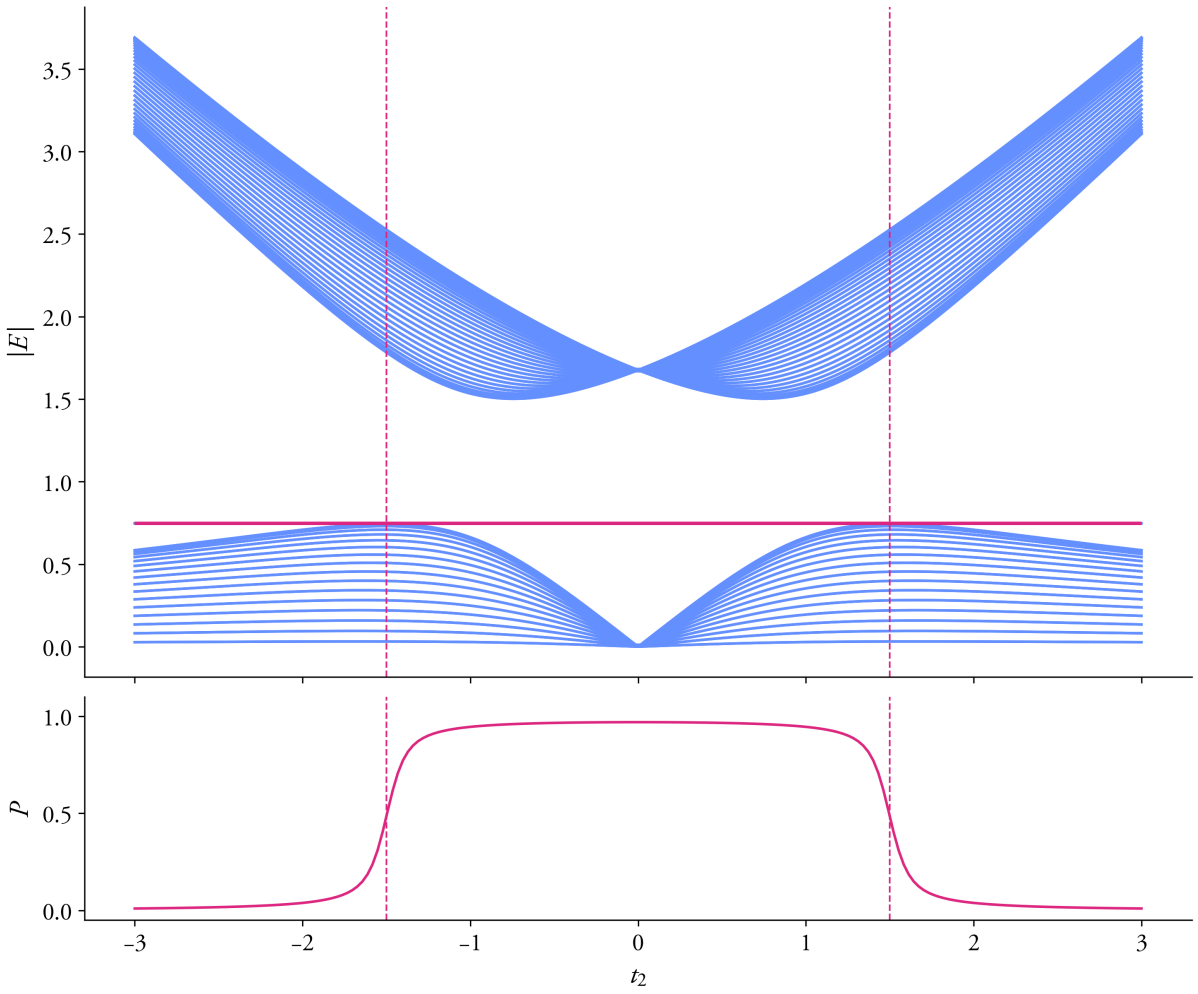

Figure 3.5: The absolute value of the energy spectrum of the SSH3 model of 98 sites, open boundary conditions, and evaluated at $t_1 = 0.9$, $t_2 = 1.1$, $t_3 = 1.5$, and $\gamma = 0.5$. The transition points are marked with vertical lines. The lower panel shows the biorthogonal polarization.

rework the q term as

$$\begin{aligned} q &= -(t_1+\gamma)t_2t_3e^{ik} - (t_1-\gamma)t_2t_3e^{-ik} \\ &= -t_2t_3\left[(t_1+\gamma)e^{ik} + (t_1-\gamma)e^{-ik}\right] \\ &= -t_2t_3\left[2t_1\cos k + i2\gamma\sin k\right]. \end{aligned} \tag{3.4}$$

The discriminant is given by

$$\begin{aligned} \Delta &= -(4p^3 + 27q^2) \\ &= 4(t_1^2+t_2^2+t_3^2-\gamma^2)^3 - 27t_2^2t_3^2\left(2t_1\cos k + i2\gamma\sin k\right)^2. \end{aligned}$$

A repeated eigenvalue is guaranteed when the discriminant is zero. The discriminant is split into real and imaginary parts, $\Delta = \Delta_r + i\Delta_i$. The real part is given by

$$4(t_1^2+t_2^2+t_3^2-\gamma^2)^3 + 108t_2^2t_3^2\left(\gamma^2\sin^2 k - t_1^2\cos^2 k\right),$$

and the imaginary part is given by

$$-i108t_2^2t_3^2t_1\gamma\sin 2k.$$

Repeated eigenvalues require that both the real and imaginary parts are zero. The imaginary part shows that this is only possible when at least one of t_1, t_2, t_3, $\sin 2k$, and γ is zero. Each of these cases will be considered separately, ignoring the Hermitian case $\gamma = 0$, as exceptional points are a non-Hermitian phenomenon.

The case of $t_3 = 0$ eliminates the dependence on k in the Bloch Hamiltonian. Point chiral symmetry, defined in Equation 3.2, therefore becomes $SH(k)S^{-1} = -H(\pi + k) = -H(k)$. In other words, SLS is introduced to the Hamiltonian, and all eigenvalues must come in $\pm E$ pairs according to the energy constraint presented in Table 2.1. It follows that at least one of the three eigenstates has the eigenvalue 0, while the remaining two appear in a $\pm\epsilon$ pair. Solving Equation 3.3 for the exact solutions gives

$$\begin{aligned} E_1 &= 0, \\ E_2 &= -\sqrt{-\gamma^2 + t_1^2 + t_2^2}, \\ E_3 &= \sqrt{-\gamma^2 + t_1^2 + t_2^2}. \end{aligned}$$

The solutions show that EP2s are not possible for $t_3 = 0$. EP3s, on the other hand, may be found when the last two eigenvalues also are zero, which happens when

$$t_1^2 + t_2^2 = \gamma^2. \tag{3.5}$$

The EP3 thus forms a circle with radius γ in the $t_1 - t_2$ plane of the parameter space, with $t_3 = 0$. However, since non-Hermitian matrices may have linearly independent eigenvectors with the same eigenvalue, it may be that only parts of this circle are genuine exceptional points. The Jordan form of the Bloch Hamiltonian after the substitutions $t_3 = 0$ and $t_2 = \pm\sqrt{\gamma^2 - t_1^2}$ is given by

$$\begin{pmatrix} 0 & 1 & 0 \\ 0 & 0 & 1 \\ 0 & 0 & 0 \end{pmatrix}.$$

The geometric multiplicity of the eigenvalue 0 is 1, and the entire circle in parameter space thereby represents an EP3.

For $t_2 = 0$, Equation 3.3 again loses its k-dependence. SLS is now introduced through the unitary transformation $U = \mathrm{diag}(-1, 1, 1)$:

$$\begin{pmatrix} -1 & 0 & 0 \\ 0 & 1 & 0 \\ 0 & 0 & 1 \end{pmatrix} \begin{pmatrix} 0 & t_1 + \gamma & t_3 e^{-ik} \\ t_1 - \gamma & 0 & 0 \\ t_3 e^{ik} & 0 & 0 \end{pmatrix} \begin{pmatrix} -1 & 0 & 0 \\ 0 & 1 & 0 \\ 0 & 0 & 1 \end{pmatrix} = - \begin{pmatrix} 0 & t_1 + \gamma & t_3 e^{-ik} \\ t_1 - \gamma & 0 & 0 \\ t_3 e^{ik} & 0 & 0 \end{pmatrix}.$$

It follows from the interchangeability of t_2 and t_3 in Equation 3.3 that the eigenvalue solutions are the same as for the previous case after the transformation $t_2 \to t_3$. The solutions are thus given by

$$\begin{aligned} E_1 &= 0, \\ E_2 &= -\sqrt{-\gamma^2 + t_1^2 + t_3^2}, \\ E_3 &= \sqrt{-\gamma^2 + t_1^2 + t_3^2}. \end{aligned}$$

The Jordan form is also the same, meaning that another circular EP3 loop exists in the parameter space, this time in the $t_1 - t_3$ plane.

When $t_1 = 0$, the Bloch Hamiltonian is given by

$$H(k) = \begin{pmatrix} 0 & \gamma & t_3 e^{-ik} \\ -\gamma & 0 & t_2 \\ t_3 e^{ik} & t_2 & 0 \end{pmatrix}. \tag{3.6}$$

Chiral symmetry can be observed in the matrix above as $UH^{\dagger}(k)U = -H(k)$ for the unitary matrix $U = \text{diag}(-1, -1, 1)$. For the SSH3 chain, this energy constraint means that at least one of the eigenvalues is purely imaginary. The possibilities of EPs are therefore either EP3s, where all eigenvalues are purely imaginary, or EP2s where the eigenvalue pair becomes purely imaginary and distinct from the third eigenvalue. For an EP3 with a purely imaginary eigenvalue $E = i\epsilon$ with $\epsilon \in \mathbb{R}$, the trace of the matrix must be $i3\epsilon$ and the determinant $-i\epsilon^3$. Since the trace of the matrix is 0, we find that this is only possible when all eigenvalues are zero. As the determinant is equivalent to $-q$ as defined in Equation 3.4, zero eigenvalues are only possible if

$$2it_2t_3\gamma \sin k = 0. \tag{3.7}$$

The cases of t_2 and t_3 being zero have already been considered. Solutions to $\sin k = 0$ form a subset of the solutions to $\sin 2k$, which is the next general case that zeroes the imaginary part of the discriminant; more on this in the next paragraph. As for EP2s, the eigenvalues can be written as $i\epsilon$ and $i\lambda$ for $\epsilon \neq \lambda$ and where $i\epsilon$ has an algebraic multiplicity of 2. The sum of eigenvalues is $i(2\epsilon + \lambda)$, meaning $\lambda = -2\epsilon$ by the Hamiltonian's zero trace. After relating the product of eigenvalues, $-i\lambda(\epsilon^2) = i2\epsilon^3$ to the q-term above,

$$\epsilon^3 = t_2t_3\gamma \sin k.$$

The eigenvalues are therefore

$$E_1 = -2(t_2t_3\gamma \sin k)^{\frac{1}{3}}, \quad E_2, E_3 = (t_2t_3\gamma \sin k)^{\frac{1}{3}}.$$

To find the parameter space where these occur, we return to the discriminant. After simplifications, the real part presented in Equation 3.5 is given by

$$(t_2^2 + t_3^2 - \gamma^2)^3 + 27t_2^2t_3^2\gamma^2 \sin^2 k = 0.$$

The imaginary part is trivially zero due to $t_1 = 0$. Equation 3.5 consequently defines a curve in parameter space where these EP2s occur. Isolating t_2, t_3, or γ from the above constraint gives a cubic in terms of each respective parameter squared. Exact solutions thereby exist, but these are lengthy and will not be presented here. Notably, solutions belong to the strong non-Hermitian regime, as γ must be larger than t_2 and t_3 for real solutions.

Turning to the case where $\sin 2k = 0$, we consider $k = n\pi$ and $k = (n + \frac{1}{2})\pi$ for $n \in \mathbb{Z}$ separately. In the first case, the Bloch Hamiltonian becomes

$$H_{\pm}(k) = \begin{pmatrix} 0 & t_1 + \gamma & \pm t_3 \\ t_1 - \gamma & 0 & t_2 \\ \pm t_3 & t_2 & 0 \end{pmatrix}. \tag{3.8}$$

The subscript denotes the sign of $\cos k$ for the choice of k. Since all matrix elements are real, the Hamiltonian exhibits PT-symmetry. The eigenvalues are therefore either real or come in pairs of complex conjugates. By the combined effect of PT- and TRS, the energies must satisfy the constraint $\{\varepsilon(k)\} = \{\varepsilon(-k)\}$, implying that $H_+(k)$ and $H_-(k)$ share eigenvalues. Further, a unitary transform exits such that $UH_+(k)U^{-1} = -H_-(k)$, providing the additional constraint of $\{\varepsilon(k)\} = \{-\varepsilon(-k)\}$. The combined energy constraint therefore requires $\{\varepsilon(k)\} = \{-\varepsilon(k)\}$. With a total of three eigenvalues, at least one eigenvalue has to be zero. All solutions thereby require a zero determinant. In other words,

$$\pm 2t_1t_2t_3 = 0. \tag{3.9}$$

All solutions to this equation have been considered in the previous sections. If $k = (n + \frac{1}{2})\pi$, the Bloch Hamiltonian instead takes the form

$$H(k) = \begin{pmatrix} 0 & t_1 + \gamma & \pm it_3 \\ t_1 - \gamma & 0 & t_2 \\ \mp it_3 & t_2 & 0 \end{pmatrix}. \tag{3.10}$$

In this case, the matrix exhibits PHS through the unitary transformation $U = \mathrm{diag}(1, -1, 1)$:

$$\begin{pmatrix} 1 & 0 & 0 \\ 0 & -1 & 0 \\ 0 & 0 & 1 \end{pmatrix} \begin{pmatrix} 0 & t_1 + \gamma & \pm i t_3 \\ t_1 - \gamma & 0 & t_2 \\ \mp i t_3 & t_2 & 0 \end{pmatrix} \begin{pmatrix} 1 & 0 & 0 \\ 0 & -1 & 0 \\ 0 & 0 & 1 \end{pmatrix} = - \begin{pmatrix} 0 & t_1 + \gamma & \pm i t_3 \\ t_1 - \gamma & 0 & t_2 \\ \mp i t_3 & t_2 & 0 \end{pmatrix}.$$

Hence, the eigenvalues are either purely imaginary or come in pairs of opposite-sign real parts and equal imaginary parts. With eigenvalues $a + bi$, $-a + bi$, and $i\lambda$, the determinant can be written as $-(b^2 + a^2)\lambda$. For an EP to be possible, a has to be zero. Further, because of the zero trace of the Hamiltonian, $2bi + \lambda i = 0$. An EP3 is thereby only possible when all eigenvalues are zero, which is the case when the determinant is zero:

$$\pm 2 t_1 t_2 t_3 = 0. \tag{3.11}$$

The solutions to this equation have already been discussed. An EP2, however, yields the relationship

$$i2b^3 = \pm i2 t_2 t_3 \gamma. \tag{3.12}$$

Whether the right-hand side is positive or negative depends on the sign of $\sin k$. Turning to the real part of the discriminant, the necessary condition for repeating eigenvalues is

$$(t_1^2 + t_2^2 + t_3^2 - \gamma^2)^3 + 27 t_2^2 t_3^2 \gamma^2 = 0. \tag{3.13}$$

The second term is always positive, which means that the first term must be negative for real solutions. Since the only negative term inside the first term is $-\gamma^2$, these EPs belong to a strongly NH regime.

Figures 3.6, 3.7, and 3.8 were made to numerically visualize the EPs. An EP3 is characterized by an eigenvector overlap of 1 between all three normalized eigenvectors. As such, they may be (approximately) found through spatial discretization of the parameter space and the subsequent calculation of the minimal overlap between the eigenvectors. The trivial overlap of a vector with itself was excluded for computational purposes. It is possible to extend this procedure to capture both EP2s and EP3s in the plot. This is done by instead calculating the minimal overlap between the eigenvectors. Again, the overlap with itself was excluded, since this is trivially 1.

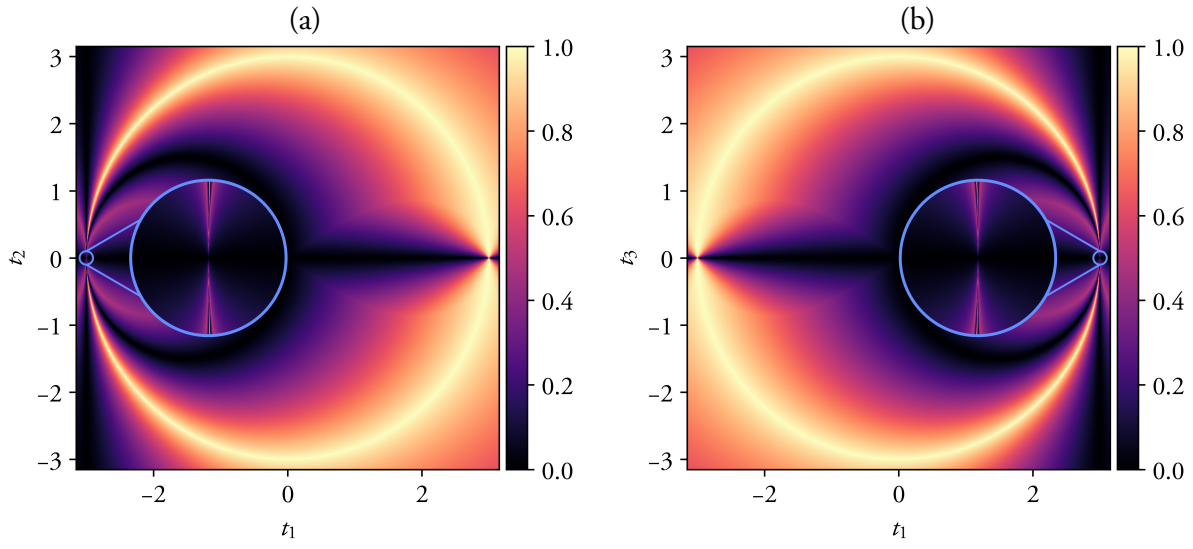

Figure 3.6: A numerical visualization of EP3s in the SSH3 chain with $\gamma = 3$, $k = 1$, and (a) $t_3 = 0$ and (b) $t_2 = 0$. Both images include enlargements of regions where the EP3s are harder to distinguish. The EP3s are represented as the minimum overlap between the normalized eigenvectors, $\min_{i \neq j}(\phi_i \cdot \phi_j)$.

In Figure 3.6, the circular EP3s derived from the cases $t_3 = 0$ and $t_2 = 0$ are observed. For both cases, a region exists where it is not evident that EP3s are present. This, however, is a manifestation of numerical limitations,

as suggested by the enlargements in the figure; the EP3s are visible to the extent that the numerical resolution permits it. We may further show that the EP3s are indeed EP3s by exact calculations for the specific cases in question. For $t_3 = 0$, the questionable region happens for around negative solution for t_1 at $t_2 = 0$, which has an exact solution given by Equation 3.5. Figure 3.7 shows the particle-hole symmetric case, where two EP3s are connected via EP2 lines; this is supported by previous research [25]. The same feature is observed in the chiral symmetric case, $t_1 = 0$, illustrated in Figure 3.8.

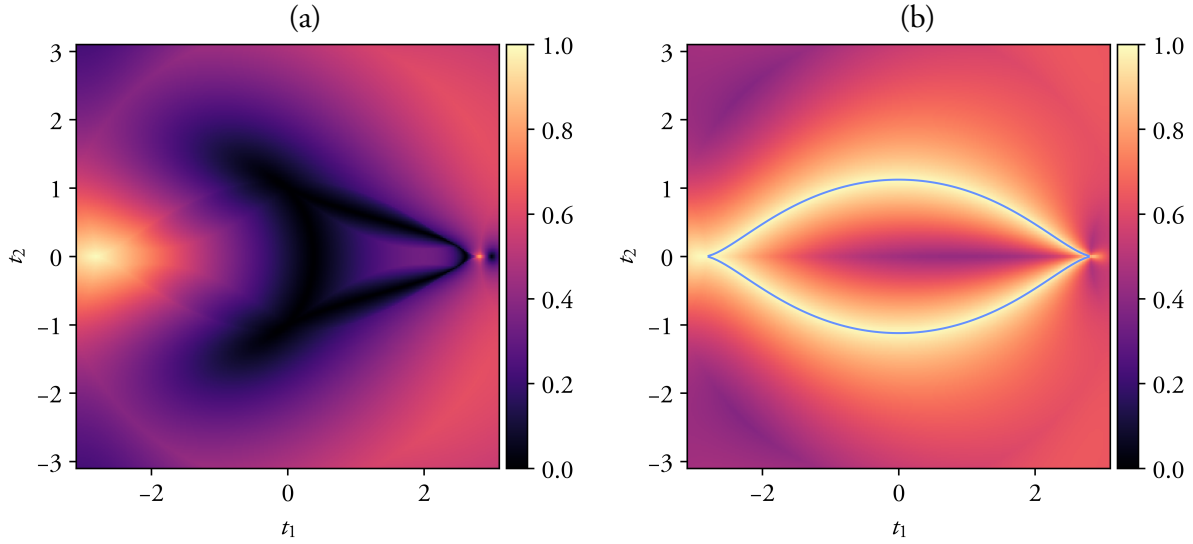

Figure 3.7: A numerical visualization of EP3s and EP2s in the SSH3 chain with $t_3 = 1$ and $\gamma = 3$ at $k = -\pi/2$. (a) EP3s represented as the minimum overlap between the normalized eigenvectors, $\min_{i \neq j}(\phi_i \cdot \phi_j)$. (b) All EPs represented as the maximum overlap between the normalized eigenvectors, $\max_{i \neq j}(\phi_i \cdot \phi_j)$. The blue lines represent exact solutions to Equation 3.5.

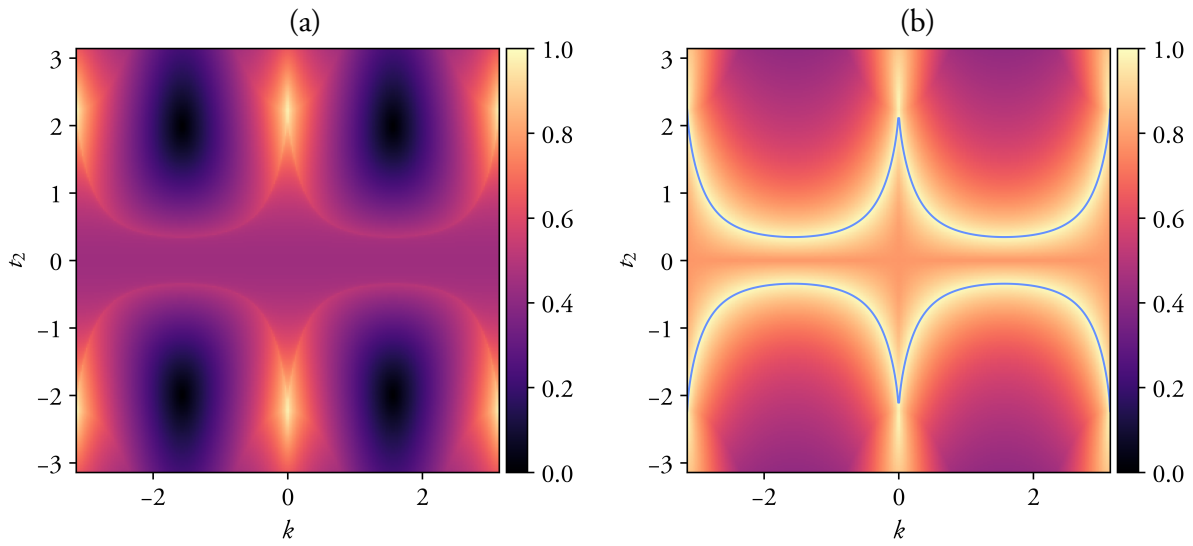

Figure 3.8: A numerical visualization of EP3s and EP2s in the SSH3 chain with $t_1 = 0$, $t_3 = 2$, and $\gamma = 3$. (a) EP3s represented as the minimum overlap between the normalized eigenvectors, $\min_{i \neq j}(\phi_i \cdot \phi_j)$. (b) All EPs represented as the maximum overlap between the normalized eigenvectors, $\max_{i \neq j}(\phi_i \cdot \phi_j)$. The blue lines represent exact solutions to Equation 3.13.

3.6 The Lee transformation

The NH skin effect is obvious in the case of anisotropy, as this introduces a preferred direction in the lattice. However, the skin effect can also occur in systems with reciprocal couplings. In this section, a reciprocal model related to the SSH3 chain is introduced, where all of our earlier findings are expected to hold. Hence, the new model provides another path to experimental validation of our results.

The Bloch Hamiltonian of the SSH3 model can be transformed by the unitary transformation

$$U = \frac{1}{\sqrt{2}} \begin{pmatrix} 1 & i & 0 \\ i & 1 & 0 \\ 0 & 0 & \sqrt{2} \end{pmatrix}. \tag{3.14}$$

The transformed Hamiltonian is given by

$$H'(k) = UH(k)U^\dagger = \begin{pmatrix} i\gamma & t_1 & \frac{-it_2+t_3e^{-ik}}{\sqrt{2}} \\ t_1 & -i\gamma & \frac{t_2-it_3e^{-ik}}{\sqrt{2}} \\ \frac{it_2+t_3e^{ik}}{\sqrt{2}} & \frac{t_2+it_3e^{ik}}{\sqrt{2}} & 0 \end{pmatrix}. \tag{3.15}$$

Because the transformation is unitary, the new Hamiltonian has the same eigenvalues as the original SSH3 Hamiltonian. The resultant lattice is depicted in Figure 3.9. The transformation is inspired by the transformation of the regular non-Hermitian SSH chain into the Lee model [8], and will therefore be referred to as the Lee3 model. For the sake of brevity, new hopping amplitudes are introduced, defined by

$$t_2' = \frac{t_2}{\sqrt{2}}, \quad t_3' = \frac{t_3}{\sqrt{2}}.$$

After transforming the Hamiltonian above back to the spatial basis, we find that with $M = 2$, the Hamiltonian is given by

$$H' = \begin{pmatrix} i\gamma & t_1 & -it_2' & 0 & 0 & t_3' \\ t_1 & -i\gamma & t_2' & 0 & 0 & -it_3' \\ it_2' & t_2' & 0 & t_3' & it_3' & 0 \\ 0 & 0 & t_3' & i\gamma & t_1 & -it_2' \\ 0 & 0 & -it_3' & t_1 & -i\gamma & t_2' \\ t_3' & it_3' & 0 & it_2' & t_2' & 0 \end{pmatrix}. \tag{3.16}$$

In Equation 3.16, we have periodic boundary conditions. More generally, the Hamiltonian can be written with M unit cells as

$$H' = \sum_{m=1}^{M} \left(i\gamma c_{m,A}^\dagger c_{m,A} - i\gamma c_{m,B}^\dagger c_{m,B} \right) + \sum_{m=1}^{M} \left(t_1 c_{m,A}^\dagger c_{m,B} + it_2' c_{m,C}^\dagger c_{m,A} + t_2' c_{C,m}^\dagger c_{B,m} + h.c. \right) + \sum_{m=1}^{M-1} \left(t_3' c_{m+1,A}^\dagger c_{m,C} - it_3' c_{m+1,B}^\dagger c_{m,C} + h.c. \right).$$

Since the transformation is unitary, the energy spectrum will be the same as for the SSH3 chain. Hence, the same topological phases are expected, with boundary states related to the SSH3 chain by the unitary transformation. In the spatial basis, the transformation is simply $\oplus_{m=1}^{M} U$, where U is the unitary transformation defined above. Because of the local nature of the transformation, acting within each unit cell, the non-Hermitian skin effect is preserved. This is illustrated in Figure 3.10, where the average site amplitudes for all eigenstates are shown.

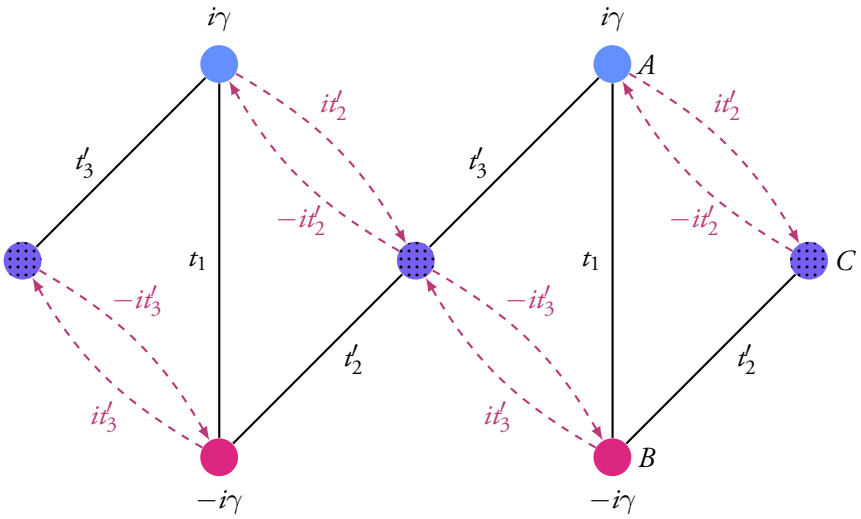

Figure 3.9: An illustration of the Lee3 chain structure.

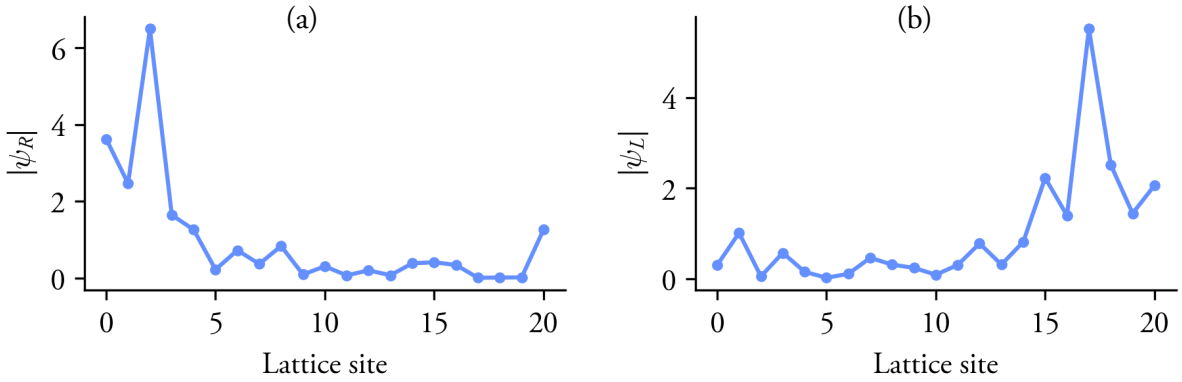

Figure 3.10: The non-Hermitian skin effect for (a) right and (b) left eigenstates of the Lee3 model with $N = 21$, $t_1 = 0.9$, $t_2 = 1.1$, $t_3 = 3$ and $\gamma = 0.5$. The spatial profile is defined as the absolute value of the lattice-site amplitudes.

4 Conclusion and outlook

In this work, the trimer SSH chain with anisotropic hopping amplitudes was studied in the biorthogonal context. A general lattice with exact boundary states was introduced, through which approximate boundary states could be derived for the SSH3 chain of different lengths. It was demonstrated that the conventional BBC is broken for the SSH3 chain, but that it nevertheless exhibits topological phases that appear well-predicted by biorthogonal polarization. Hence, BBC can be effectively restored by adopting the biorthogonal framework. The results are limited in the cases of $3M$ and $3M + 1$ lattice sites, as the boundary state ansatz sometimes fails to describe either the left or right eigenstate. Still, the biorthogonal polarization calculated using the ansatz shows good agreement with our numerical results. For a more comprehensive description, a closer examination of the eigenstate form in these cases is needed. Since the biorthogonal bulk condition calculated with the ansatz presented in this work appears valid, it would perhaps be possible to consider the $3M$ and $3M + 1$ cases as perturbations to the $3M - 1$ case, where this said ansatz is exact.

The thesis has also shown that SSH3 exhibits the NH skin effect, and that, in addition to their distinct spatial profiles, the bulk and boundary states can be distinguished by their biorthogonal projection onto the lattice sites. While the presence of the NH skin effect is trivial for a chain with anisotropic hopping, it was shown to also be present in the Lee3 model, which features reciprocal hopping amplitudes. Additionally, an exhaustive EP analysis was performed, revealing the presence of EP2s and EP3s in the SSH3 chain. The EPs were found in the strong NH regime, and their presence was confirmed by numerical visualization. The EPs have analytical solutions as their existence is reducible to cubic equations; this makes the SSH3 model interesting for studying, and potentially experimentally utilizing, EPs. It was shown that the EP3s occur for parameter values that introduce SLS or chiral symmetry. The presence of such symmetries permits winding numbers to be defined, which could characterize topological phases. This is a potential direction for further research. Another important feature that remains to be studied is the dispersion around the EPs.

The results of this work suggest several more directions for further research. With the present understanding of the anisotropic SSH3 chain, it would be interesting to generalize the results to SSH variants with more lattice sites per unit cell. By symmetry considerations, one may expect lattices with an odd number of sites to exhibit similar behavior to the SSH3. Further, while this thesis has focused on the biorthogonal BBC, one could contrast the results with the generalized Brillouin zone approach. Another line of inquiry is whether all systems that exhibit the NH skin effect are related to anisotropic models like the SSH3 chain. The Lee3 lattice presented in this work provides an example of such a connection, but it remains to be seen whether this is a general feature.

Experimental realizations of the SSH3 chain could be achieved in photonic coupled waveguides [37], topolectrical circuits [38], and single-photon interferometry [39]. He et al. [40] further propose experimental feasibility of the Hermitian SSH3 chain in the context of cold atoms. An experimental realization of the SSH3 chain would provide a platform for testing the theoretical results presented in this work and could lead to an improved understanding of its non-Hermitian physics.

References

[1] K. v. Klitzing, G. Dorda and M. Pepper, 'New Method for High-Accuracy Determination of the Fine-Structure Constant Based on Quantized Hall Resistance,' *Physical Review Letters*, vol. 45, no. 6, pp. 494–497, 11th Aug. 1980. DOI: 10.1103/PhysRevLett.45.494. [Online]. Available: https://link.aps.org/doi/10.1103/PhysRevLett.45.494.

[2] The Royal Swedish Academy of Sciences. 'The Nobel Prize in Physics 1985,' NobelPrize.org. (16th Oct. 1985), [Online]. Available: https://www.nobelprize.org/prizes/physics/1985/press-release/.

[3] M. Kohmoto, 'Topological invariant and the quantization of the Hall conductance,' *Annals of Physics*, vol. 160, no. 2, pp. 343–354, 1st Apr. 1985, ISSN: 0003-4916. DOI: 10.1016/0003-4916(85)90148-4. [Online]. Available: https://www.sciencedirect.com/science/article/pii/0003491685901484.

[4] J. E. Moore, 'The birth of topological insulators,' *Nature*, vol. 464, no. 7286, pp. 194–198, Mar. 2010, ISSN: 1476-4687. DOI: 10.1038/nature08916. [Online]. Available: https://www.nature.com/articles/nature08916.

[5] Y. Ando. 'Topological Insulators.' arXiv: 2307.14196 [cond-mat]. (26th Jul. 2023), [Online]. Available: http://arxiv.org/abs/2307.14196, preprint.

[6] M. Toriyama and G. J. Snyder. 'Are Topological Insulators Promising Thermoelectrics?' (6th Nov. 2023), [Online]. Available: https://chemrxiv.org/engage/chemrxiv/article-details/6545ba97c573f893f1c4221d, preprint.

[7] D. Smirnova, A. Tripathi, S. Kruk *et al.*, 'Room-temperature lasing from nanophotonic topological cavities,' *Light: Science & Applications*, vol. 9, no. 1, p. 127, 20th Jul. 2020, ISSN: 2047-7538. DOI: 10.1038/s41377-020-00350-3. [Online]. Available: https://www.nature.com/articles/s41377-020-00350-3.

[8] E. J. Bergholtz, J. C. Budich and F. K. Kunst, 'Exceptional topology of non-Hermitian systems,' *Reviews of Modern Physics*, vol. 93, no. 1, p. 015 005, 24th Feb. 2021. DOI: 10.1103/RevModPhys.93.015005. [Online]. Available: https://link.aps.org/doi/10.1103/RevModPhys.93.015005.

[9] Y. Ashida, Z. Gong and M. Ueda, 'Non-Hermitian Physics,' *Advances in Physics*, vol. 69, no. 3, pp. 249–435, 2nd Jul. 2020, ISSN: 0001-8732, 1460-6976. DOI: 10.1080/00018732.2021.1876991. arXiv: 2006.01837 [cond-mat, physics:quant-ph]. [Online]. Available: http://arxiv.org/abs/2006.01837.

[10] S. Weidemann, M. Kremer, T. Helbig *et al.*, 'Topological funneling of light,' *Science*, vol. 368, no. 6488, pp. 311–314, 17th Apr. 2020. DOI: 10.1126/science.aaz8727. [Online]. Available: https://www.science.org/doi/10.1126/science.aaz8727.

[11] B. Peng, Ş. K. Özdemir, F. Lei *et al.*, 'Parity–time-symmetric whispering-gallery microcavities,' *Nature Physics*, vol. 10, no. 5, pp. 394–398, May 2014, ISSN: 1745-2481. DOI: 10.1038/nphys2927. [Online]. Available: https://www.nature.com/articles/nphys2927.

[12] W. Chen, Ş. Kaya Özdemir, G. Zhao, J. Wiersig and L. Yang, 'Exceptional points enhance sensing in an optical microcavity,' *Nature*, vol. 548, no. 7666, pp. 192–196, Aug. 2017, ISSN: 1476-4687. DOI: 10.1038/nature23281. [Online]. Available: https://www.nature.com/articles/nature23281.

[13] H. Hodaei, A. U. Hassan, S. Wittek *et al.*, 'Enhanced sensitivity at higher-order exceptional points,' *Nature*, vol. 548, no. 7666, pp. 187–191, Aug. 2017, ISSN: 1476-4687. DOI: 10.1038/nature23280. [Online]. Available: https://www.nature.com/articles/nature23280.

[14] C. Han, M. Lee, S. Callard, C. Seassal and H. Jeon, 'Lasing at topological edge states in a photonic crystal L3 nanocavity dimer array,' *Light: Science & Applications*, vol. 8, no. 1, p. 40, 24th Apr. 2019, ISSN: 2047-7538. DOI: 10.1038/s41377-019-0149-7. [Online]. Available: https://www.nature.com/articles/s41377-019-0149-7.

[15] L. Thatcher, P. Fairfield, L. Merlo-Ramírez and J. Merlo, 'Experimental observation of topological phase transitions in a mechanical 1D-SSH model,' *Physica Scripta*, vol. 97, 10th Feb. 2022. DOI: 10.1088/1402-4896/ac4ed2.

[16] Y. He and C.-C. Chien, 'Non-Hermitian generalizations of extended Su–Schrieffer–Heeger models,' *Journal of Physics: Condensed Matter*, vol. 33, no. 8, p. 085 501, Dec. 2020, ISSN: 0953-8984. DOI: 10.1088/1361-648X/abc974. [Online]. Available: https://dx.doi.org/10.1088/1361-648X/abc974.

[17] A. Altland and M. R. Zirnbauer, 'Nonstandard symmetry classes in mesoscopic normal-superconducting hybrid structures,' *Physical Review B*, vol. 55, no. 2, pp. 1142–1161, 1st Jan. 1997. DOI: 10.1103/PhysRevB.55.1142. [Online]. Available: https://link.aps.org/doi/10.1103/PhysRevB.55.1142.

[18] D. Tong. 'Discrete Symmetries,' Lectures on Applications of Quantum Mechanics. (2023), [Online]. Available: https://www.damtp.cam.ac.uk/user/tong/aqm.html.

[19] M. Dresselhaus, *Group Theory*, 1st ed. Heidelberg: Springer Berlin, 18th Dec. 2007, 582 pp., ISBN: 978-3-540-32899-5. [Online]. Available: https://link.springer.com/book/10.1007/978-3-540-32899-5.

[20] E. P. Wigner, 'Normal Form of Antiunitary Operators,' *Journal of Mathematical Physics*, vol. 1, no. 5, pp. 409–413, 22nd Dec. 2004, ISSN: 0022-2488. DOI: 10.1063/1.1703672. [Online]. Available: https://doi.org/10.1063/1.1703672.

[21] K. Kawabata, K. Shiozaki, M. Ueda and M. Sato, 'Symmetry and Topology in Non-Hermitian Physics,' *Physical Review X*, vol. 9, no. 4, p. 041 015, 21st Oct. 2019. DOI: 10.1103/PhysRevX.9.041015. [Online]. Available: https://link.aps.org/doi/10.1103/PhysRevX.9.041015.

[22] R. Zhang, H. Qin and J. Xiao, 'PT-symmetry entails pseudo-Hermiticity regardless of diagonalizability,' *Journal of Mathematical Physics*, vol. 61, no. 1, p. 012 101, 1st Jan. 2020, ISSN: 0022-2488, 1089-7658. DOI: 10.1063/1.5117211. arXiv: 1904.01967 [math-ph, physics:physics, physics:quant-ph]. [Online]. Available: http://arxiv.org/abs/1904.01967.

[23] C. M. Bender and S. Boettcher, 'Real Spectra in Non-Hermitian Hamiltonians Having $\mathsc{P}\mathsc{T}$ Symmetry,' *Physical Review Letters*, vol. 80, no. 24, pp. 5243–5246, 15th Jun. 1998. DOI: 10.1103/PhysRevLett.80.5243. [Online]. Available: https://link.aps.org/doi/10.1103/PhysRevLett.80.5243.

[24] A. Regensburger, C. Bersch, M.-A. Miri, G. Onishchukov, D. N. Christodoulides and U. Peschel, 'Parity–time synthetic photonic lattices,' *Nature*, vol. 488, no. 7410, pp. 167–171, Aug. 2012, ISSN: 1476-4687. DOI: 10.1038/nature11298. [Online]. Available: https://www.nature.com/articles/nature11298.

[25] A. Montag and F. K. Kunst. 'Symmetry-induced higher-order exceptional points in two dimensions.' arXiv: 2401.10913 [cond-mat, physics:physics, physics:quant-ph]. (21st Feb. 2024), [Online]. Available: http://arxiv.org/abs/2401.10913, preprint.

[26] F. K. Kunst, G. van Miert and E. J. Bergholtz, 'Boundaries of boundaries: A systematic approach to lattice models with solvable boundary states of arbitrary codimension,' *Physical Review B*, vol. 99, no. 8, p. 085 426, 19th Feb. 2019. DOI: 10.1103/PhysRevB.99.085426. [Online]. Available: https://link.aps.org/doi/10.1103/PhysRevB.99.085426.

[27] E. Edvardsson, F. K. Kunst, T. Yoshida and E. J. Bergholtz, 'Phase transitions and generalized biorthogonal polarization in non-Hermitian systems,' *Physical Review Research*, vol. 2, no. 4, p. 043 046, 8th Oct. 2020, ISSN: 2643-1564. DOI: 10.1103/PhysRevResearch.2.043046. [Online]. Available: https://link.aps.org/doi/10.1103/PhysRevResearch.2.043046.

[28] D. J. Griffiths and D. F. Schroeter. 'Introduction to Quantum Mechanics,' Higher Education from Cambridge University Press. (16th Aug. 2018), [Online]. Available: https://www.cambridge.org/highereducation/books/introduction-to-quantum-mechanics/990799CA07A83FC5312402AF6860311E quantum-dynamics/1B602640833228F3A51653D489AC566F.

[29] D. C. Brody, 'Biorthogonal quantum mechanics,' *Journal of Physics A: Mathematical and Theoretical*, vol. 47, no. 3, p. 035 305, Dec. 2013, ISSN: 1751-8121. DOI: 10.1088/1751-8113/47/3/035305. [Online]. Available: https://dx.doi.org/10.1088/1751-8113/47/3/035305.

[30] S. D. Deshpande and R. B. Pode, 'Matrix representation of vectors and operators in nonorthogonal basis vectors,' *American Journal of Physics*, vol. 56, no. 4, pp. 362–365, 1st Apr. 1988, ISSN: 0002-9505. DOI: 10.1119/1.15614. [Online]. Available: https://doi.org/10.1119/1.15614.

[31] S. Yao and Z. Wang, 'Edge States and Topological Invariants of Non-Hermitian Systems,' *Physical Review Letters*, vol. 121, no. 8, p. 086 803, 21st Aug. 2018. DOI: 10.1103/PhysRevLett.121.086803. [Online]. Available: https://link.aps.org/doi/10.1103/PhysRevLett.121.086803.

[32] F. K. Kunst, E. Edvardsson, J. C. Budich and E. J. Bergholtz, 'Biorthogonal Bulk-Boundary Correspondence in Non-Hermitian Systems,' *Physical Review Letters*, vol. 121, no. 2, p. 026 808, 11th Jul. 2018. DOI: 10.1103/PhysRevLett.121.026808. [Online]. Available: https://link.aps.org/doi/10.1103/PhysRevLett.121.026808.

[33] W. P. Su, J. R. Schrieffer and A. J. Heeger, 'Soliton excitations in polyacetylene,' *Physical Review B*, vol. 22, no. 4, pp. 2099–2111, 15th Aug. 1980. DOI: 10.1103/PhysRevB.22.2099. [Online]. Available: https://link.aps.org/doi/10.1103/PhysRevB.22.2099.

[34] C. Yin, H. Jiang, L. Li, R. Lü and S. Chen, 'Geometrical meaning of winding number and its characterization of topological phases in one-dimensional chiral non-Hermitian systems,' *Physical Review A*, vol. 97, no. 5, p. 052 115, 16th May 2018, ISSN: 2469-9926, 2469-9934. DOI: 10.1103/PhysRevA.97.052115. arXiv: 1802.04169 [cond-mat]. [Online]. Available: http://arxiv.org/abs/1802.04169.

[35] J. K. Asbóth, L. Oroszlány and A. Pályi, *A Short Course on Topological Insulators: Band-structure Topology and Edge States in One and Two Dimensions*. 2016, vol. 919. DOI: 10.1007/978-3-319-25607-8. arXiv: 1509.02295 [cond-mat]. [Online]. Available: http://arxiv.org/abs/1509.02295.

[36] A. Anastasiadis, G. Styliaris, R. Chaunsali, G. Theocharis and F. K. Diakonos, 'Bulk-edge correspondence in the trimer Su-Schrieffer-Heeger model,' *Physical Review B*, vol. 106, no. 8, p. 085 109, 5th Aug. 2022. DOI: 10.1103/PhysRevB.106.085109. [Online]. Available: https://link.aps.org/doi/10.1103/PhysRevB.106.085109.

[37] X. Zhu, H. Wang, S. K. Gupta *et al.*, 'Photonic non-Hermitian skin effect and non-Bloch bulk-boundary correspondence,' *Physical Review Research*, vol. 2, no. 1, p. 013 280, 9th Mar. 2020. DOI: 10.1103/PhysRevResearch.2.013280. [Online]. Available: https://link.aps.org/doi/10.1103/PhysRevResearch.2.013280.

[38] T. Hofmann, T. Helbig, F. Schindler *et al.*, 'Reciprocal skin effect and its realization in a topolectrical circuit,' *Physical Review Research*, vol. 2, no. 2, p. 023 265, 2nd Jun. 2020. DOI: 10.1103/PhysRevResearch.2.023265. [Online]. Available: https://link.aps.org/doi/10.1103/PhysRevResearch.2.023265.

[39] K. Wang, L. Xiao, J. C. Budich, W. Yi and P. Xue, 'Simulating Exceptional Non-Hermitian Metals with Single-Photon Interferometry,' *Physical Review Letters*, vol. 127, no. 2, p. 026 404, 9th Jul. 2021. DOI: 10.1103/PhysRevLett.127.026404. [Online]. Available: https://link.aps.org/doi/10.1103/PhysRevLett.127.026404.

[40] Y. He, K. Wright, S. Kouachi and C.-C. Chien, 'Topology, edge states, and zero-energy states of ultracold atoms in one-dimensional optical superlattices with alternating on-site potentials or hopping coefficients,' *Physical Review A*, vol. 97, no. 2, p. 023 618, 12th Feb. 2018. DOI: 10.1103/PhysRevA.97.023618. [Online]. Available: https://link.aps.org/doi/10.1103/PhysRevA.97.023618.

A Derivation of the Bloch Hamiltonian

$$
H_k = \begin{pmatrix} a(k)e^{ik} \\ b(k)e^{ik} \\ c(k)e^{ik} \\ a(k)e^{2ik} \\ b(k)e^{2ik} \\ c(k)e^{2ik} \\ \vdots \\ c(k)e^{Nik} \end{pmatrix}^{\dagger} \begin{pmatrix} 0 & t_1+\gamma & 0 & 0 & 0 & 0 & \dots & t_3 \\ t_1-\gamma & 0 & t_2 & 0 & 0 & 0 & \dots & 0 \\ 0 & t_2 & 0 & t_3 & 0 & 0 & \dots & 0 \\ 0 & 0 & t_3 & 0 & t_1+\gamma & 0 & \dots & 0 \\ 0 & 0 & 0 & t_1-\gamma & 0 & t_2 & \dots & 0 \\ 0 & 0 & 0 & 0 & t_2 & 0 & \dots & 0 \\ \vdots & \vdots & \vdots & \vdots & \vdots & \vdots & \ddots & t_2 \\ t_3 & 0 & 0 & 0 & 0 & 0 & t_2 & 0 \end{pmatrix} \begin{pmatrix} a(k)e^{ik} \\ b(k)e^{ik} \\ c(k)e^{ik} \\ a(k)e^{2ik} \\ b(k)e^{2ik} \\ c(k)e^{2ik} \\ \vdots \\ c(k)e^{Nik} \end{pmatrix}
$$

$$
= \begin{pmatrix} a^*(k)e^{-ik} \\ b^*(k)e^{-ik} \\ c^*(k)e^{-ik} \\ a^*(k)e^{-2ik} \\ b^*(k)e^{-2ik} \\ c^*(k)e^{-2ik} \\ \vdots \\ c^*(k)e^{-Nik} \end{pmatrix}^{T} \begin{pmatrix} 0 & (t_1+\gamma)e^{ik} & 0 & 0 & 0 & 0 & \dots & t_3e^{Nik} \\ (t_1-\gamma)e^{ik} & 0 & t_2e^{ik} & 0 & 0 & 0 & \dots & 0 \\ 0 & t_2e^{ik} & 0 & t_3e^{2ik} & 0 & 0 & \dots & 0 \\ 0 & 0 & t_3e^{ik} & 0 & (t_1+\gamma)e^{2ik} & 0 & \dots & 0 \\ 0 & 0 & 0 & (t_1-\gamma)e^{2ik} & 0 & t_2e^{2ik} & \dots & 0 \\ 0 & 0 & 0 & 0 & t_2e^{2ik} & 0 & \dots & 0 \\ \vdots & \vdots & \vdots & \vdots & \vdots & \vdots & \ddots & t_2e^{Nik} \\ t_3e^{ik} & 0 & 0 & 0 & 0 & 0 & t_2e^{Nik} & 0 \end{pmatrix} \begin{pmatrix} a(k) \\ b(k) \\ c(k) \\ a(k) \\ b(k) \\ c(k) \\ \vdots \\ c(k) \end{pmatrix}
$$

$$
= \begin{pmatrix} a^*(k) \\ b^*(k) \\ c^*(k) \\ a^*(k) \\ b^*(k) \\ c^*(k) \\ \vdots \\ c^*(k) \end{pmatrix}^{T} \begin{pmatrix} 0 & (t_1+\gamma) & 0 & 0 & 0 & 0 & \dots & t_3e^{(N-1)ik} \\ (t_1-\gamma) & 0 & t_2 & 0 & 0 & 0 & \dots & 0 \\ 0 & t_2 & 0 & t_3e^{ik} & 0 & 0 & \dots & 0 \\ 0 & 0 & t_3e^{-ik} & 0 & (t_1+\gamma) & 0 & \dots & 0 \\ 0 & 0 & 0 & (t_1-\gamma) & 0 & t_2 & \dots & 0 \\ 0 & 0 & 0 & 0 & t_2 & 0 & \dots & 0 \\ \vdots & \vdots & \vdots & \vdots & \vdots & \vdots & \ddots & t_2 \\ t_3e^{(1-N)ik} & 0 & 0 & 0 & 0 & 0 & t_2 & 0 \end{pmatrix} \begin{pmatrix} a(k) \\ b(k) \\ c(k) \\ a(k) \\ b(k) \\ c(k) \\ \vdots \\ c(k) \end{pmatrix}
$$

We note that $e^{Nik} = e^{2\pi j} = 1$ for all j. Hence,

$$
H_k = \begin{pmatrix} a^*(k) \\ b^*(k) \\ c^*(k) \\ a^*(k) \\ b^*(k) \\ c^*(k) \\ \vdots \\ c^*(k) \end{pmatrix}^{T} \begin{pmatrix} 0 & (t_1+\gamma) & 0 & 0 & 0 & 0 & \dots & t_3e^{-ik} \\ (t_1-\gamma) & 0 & t_2 & 0 & 0 & 0 & \dots & 0 \\ 0 & t_2 & 0 & t_3e^{ik} & 0 & 0 & \dots & 0 \\ 0 & 0 & t_3e^{-ik} & 0 & (t_1+\gamma) & 0 & \dots & 0 \\ 0 & 0 & 0 & (t_1-\gamma) & 0 & t_2 & \dots & 0 \\ 0 & 0 & 0 & 0 & t_2 & 0 & \dots & 0 \\ \vdots & \vdots & \vdots & \vdots & \vdots & \vdots & \ddots & t_2 \\ t_3e^{ik} & 0 & 0 & 0 & 0 & 0 & t_2 & 0 \end{pmatrix} \begin{pmatrix} a(k) \\ b(k) \\ c(k) \\ a(k) \\ b(k) \\ c(k) \\ \vdots \\ c(k) \end{pmatrix}
$$

However, due to the repeating elements of the vectors, it is unchanged by the following modification:

$$H_k = \begin{pmatrix} a^*(k) \\ b^*(k) \\ c^*(k) \\ a^*(k) \\ b^*(k) \\ c^*(k) \\ \vdots \\ c^*(k) \end{pmatrix}^T \begin{pmatrix} 0 & (t_1+\gamma) & t_3 e^{-ik} & 0 & 0 & 0 & \dots & 0 \\ (t_1-\gamma) & 0 & t_2 & 0 & 0 & 0 & \dots & 0 \\ t_3 e^{ik} & t_2 & 0 & 0 & 0 & 0 & \dots & 0 \\ 0 & 0 & 0 & 0 & (t_1+\gamma) & t_3 e^{-ik} & \dots & 0 \\ 0 & 0 & 0 & (t_1-\gamma) & 0 & t_2 & \dots & 0 \\ 0 & 0 & 0 & t_3 e^{ik} & t_2 & 0 & \dots & 0 \\ \vdots & \vdots & \vdots & \vdots & \vdots & \vdots & \ddots & t_2 \\ 0 & 0 & 0 & 0 & 0 & t_3 e^{ik} & t_2 & 0 \end{pmatrix} \begin{pmatrix} a(k) \\ b(k) \\ c(k) \\ a(k) \\ b(k) \\ c(k) \\ \vdots \\ c(k) \end{pmatrix}$$

The center matrix is now the same as $\bigoplus_{m=1}^{M} H(k)$ for $H(k)$ given by Equation 3.1.

B Edge states for the 3M + 1 SSH3 chain

The case of $3M+1$ sites hosts A-sites at both ends. The left end has already been treated in the $3M-1$ case, and the right end can be treated similarly to the $3M$ case. Locally, the right end maps to an XY-lattice with the hopping terms

$$\begin{aligned} h_X &= \begin{pmatrix} 0 & t_3 \\ t_3 & 0 \end{pmatrix}, \\ h_Y &= 0, \\ h^\dagger_{O;+} &= \begin{pmatrix} 0 & t_1+\gamma \end{pmatrix}, \\ h^\dagger_{U;+} &= \begin{pmatrix} 0 & t_1-\gamma \end{pmatrix}, \\ h^\dagger_{O/U;-} &= \begin{pmatrix} t_2 & 0 \end{pmatrix}. \end{aligned}$$

The eigenvalues of h_X are $E=\pm t_3$, and the LPs for the right eigenstates are found from Equation 2.5, which gives

$$r_{R,1} = -\frac{t_1-\gamma}{t_2}, \quad r_{R,2} = \frac{t_1-\gamma}{t_2}.$$

The right eigenstates are then given by

$$\begin{aligned} |\Psi_{R,1}\rangle &= \mathcal{N}_{R,1} \sum_{m=1}^{M} \left(-\frac{t_1-\gamma}{t_2}\right)^m \left(c^\dagger_{A,m} + c^\dagger_{B,m}\right)|0\rangle, \\ |\Psi_{R,2}\rangle &= \mathcal{N}_{R,2} \sum_{m=1}^{M} \left(\frac{t_1-\gamma}{t_2}\right)^m \left(c^\dagger_{A,m} - c^\dagger_{B,m}\right)|0\rangle. \end{aligned}$$

The left eigenstates are easily found following the same procedure. As h_X is Hermitian, the only difference is the LPs, which are given by Equation 2.7. The full solutions are

$$\begin{aligned} |\Psi_{L,1}\rangle &= \mathcal{N}_{L,1} \sum_{m=1}^{M} \left(-\frac{t_1+\gamma}{t_2}\right)^m \left(c^\dagger_{A,m} + c^\dagger_{B,m}\right)|0\rangle, \\ |\Psi_{L,2}\rangle &= \mathcal{N}_{L,2} \sum_{m=1}^{M} \left(\frac{t_1+\gamma}{t_2}\right)^m \left(c^\dagger_{A,m} - c^\dagger_{B,m}\right)|0\rangle. \end{aligned}$$

Both the left and right eigenstates are exact solutions in the thermodynamic limit, as long as their localization parameters are greater than 1. Further,

$$\left|r^*_{L,1} r_{R,1}\right| = \left|r^*_{L,2} r_{R,2}\right| = \left|\frac{t_1^2-\gamma^2}{t_2^2}\right|.$$

By the biorthogonal bulk condition, the transition point is predicted by $t_2 = \pm\sqrt{|t_1^2-\gamma^2|}$. Numerical results for the energy spectrum of the $3M+1$ SSH3 chain are shown in Figure B.1.

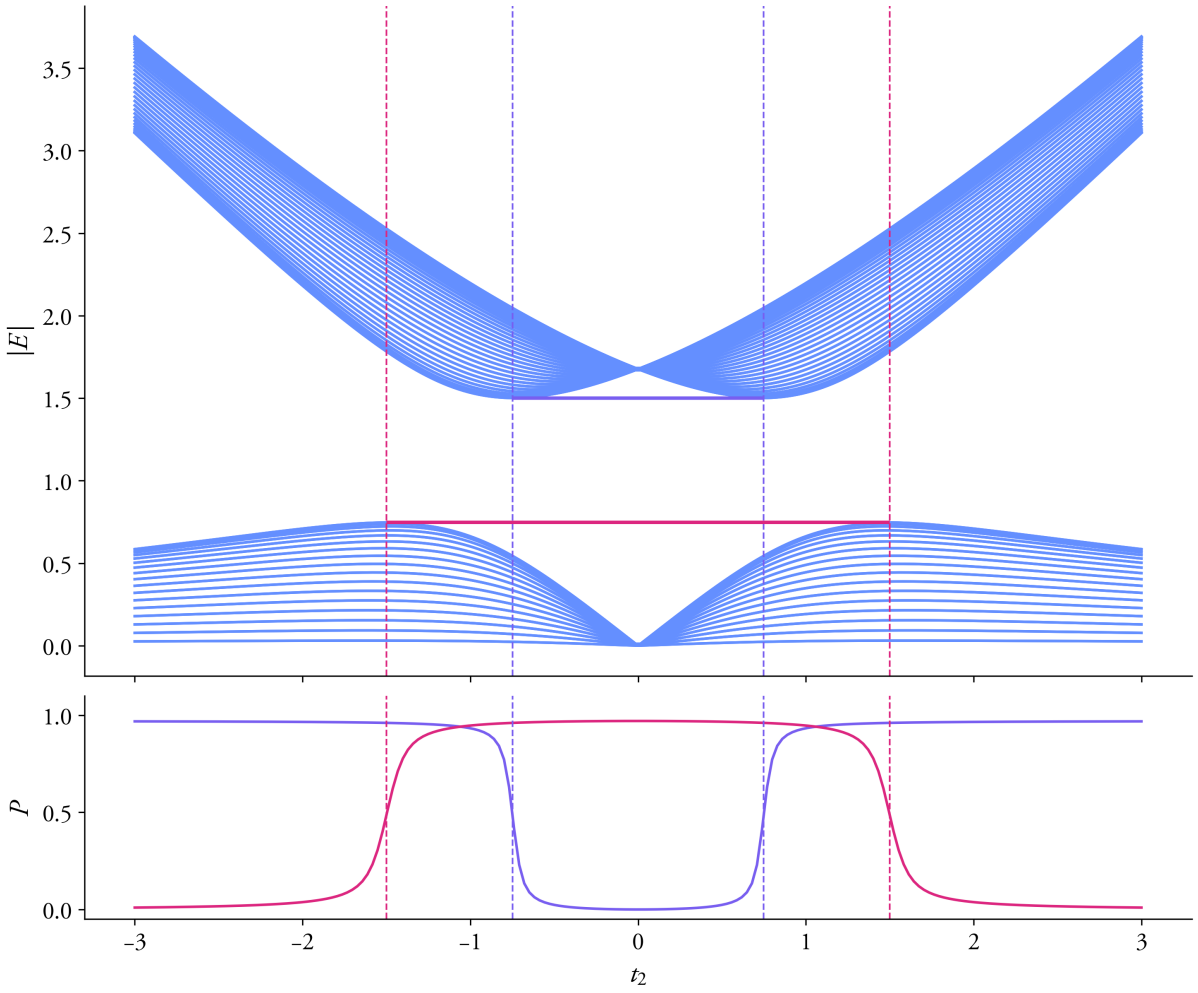

Figure B.1: The absolute value of the energy spectrum of the SSH3 model of 98 sites, open boundary conditions, and evaluated at $t_1 = 0.9$, $t_2 = 1.1$, $t_3 = 1.5$, and $\gamma = 0.5$. The transition points are marked with vertical lines. The lower panel shows the biorthogonal polarization of both types of boundary states.